



# Temperature Reduction of a Hot Component Enclosed in a Ring Filled with Power-Law Ferrofluid Under the Effect of Magnetic Field and Heat Absorption: Benefit from LBM Ability to Simulate Radiation–Convection Heat Transfer

Mohammad Nemati<sup>1</sup> · Mohammad Sefid<sup>1</sup> · Temjennaro Jamir<sup>2</sup> · Ali J. Chamkha<sup>3</sup>

Received: 10 October 2023 / Accepted: 6 December 2023  
© The Author(s), under exclusive licence to Shiraz University 2024

## Abstract

The failure to consider thermal radiation in addition to free convection heat transfer in many cases such as heat exchangers will cause an unavoidable error in the flow analysis. Due to the complexity of volumetric radiation modeling in solving various problems, it is difficult to simulate this issue, especially through computer coding. The reason for this numerical study is the lack of extensive investigation of the effect of volumetric radiation on non-Newtonian nanofluid flow under magnetic field and heat absorption. By using the LBM and simulating the natural convection phenomenon, the cooling of a square-shaped component within a sector of a ring containing a non-Newtonian nanofluid has been modeled in the present research. The findings indicate that the presence of radiation increases the average value of the Nusselt number for the shear thickening, the Newtonian, and the shear thinning fluids by about 17%, 11%, and 8.5%, respectively. The growth of the thermal performance index and the mean Nusselt Number value is observed via the enhancement of the fluid power-law index, especially in the absence of heat absorption. In most cases, the presence of nanoparticles improves the heat transfer rate, especially in cases where thermal conduction dominates convection. There is the lowest cooling performance index and magnetic field effect for the cavity placed at the angle of 45°. By designing the system in such a way that the magnetic field is imposed on the system at different angles and positions, the thermal performance can be improved to a great extent.

**Keywords** Thermal performance analysis · Cooling of a hot body · Power-law nanofluid · MHD natural convection · Volumetric radiation · Entropy generation

## List of Symbols

$\alpha$	Thermal diffusivity (m <sup>2</sup> /s)
$\beta$	Thermal expansion (1/K)
$\beta_R$	Mean absorption coefficient (1/m)
$\varepsilon$	Emissivity of radiative wall
$\sigma$	Electrical conductivity ( $\Omega$ .m)

$\sigma_R$	Scattering coefficient
$\Delta$	Heat absorption index in dimensionless form
$\lambda$	Magnetic field angle (°)
$\Gamma$	The chamber inclination angle (°)
$\theta$	Dimensionless temperature
$\varphi$	The nanoparticles volume concentration
$\zeta$	Index of thermal performance
$\tau$	Stress (pa)
$\tau_f$	Relaxation time for velocity field
$\tau_h$	Relaxation time for thermal field
$\tau_R$	Relaxation time for radiation
$\rho$	Density (kg/m <sup>3</sup> )
$\gamma$	Shear rate tensor (1/s)
$\Psi$	Dimensionless stream function
$\nu$	Kinematic viscosity (m <sup>2</sup> /s)
$\mu$	Dynamic viscosity (pa.s)
$\omega$	Weighting coefficient
$\omega_R$	Scattering albedo
$B$	The magnetic field strength (T)

✉ Mohammad Nemati  
mohammadnemati@stu.yazd.ac.ir;  
mohammadnemati.lbm@gmail.com

Mohammad Sefid  
mhsefid@yazd.ac.ir

<sup>1</sup> Faculty of Mechanical Engineering, Yazd University, Yazd, Iran

<sup>2</sup> Department of Mathematics, Kohima Science College, Jotsoma, Nagaland, India

<sup>3</sup> Faculty of Engineering, Kuwait College of Science and Technology, 35004 Doha, Kuwait

Be	The Bejan number value
$c$	Discrete velocity
$C_p$	Specific heat (J/kg K)
$D$	The position of applied magnetic field (m)
$f$	Distribution function related to the temperature field
$F$	External force (pa m <sup>2</sup> )
$g$	Gravitational acceleration (m/s <sup>2</sup> )
$G$	Incident radiation (W/m <sup>2</sup> )
$h$	Distribution function related to the temperature field
$H$	Length and height of the chamber (m)
Ha	The Hartmann number value
$I$	Particle distribution function for density radiative heat transfer
$k$	Thermal conductivity (W/m K)
$m$	Nanoparticles shape factor
$n$	Coefficient of power-law fluid
Nu	The Nusselt number
$p$	Pressure (pa)
Pr	The Prandtl number
$q$	Heat absorption coefficient (W/m <sup>3</sup> )
$\bar{q}_R$	Radiative heat flux (W/m <sup>3</sup> )
Ra	The Rayleigh number value
RP	Radiation parameter
$\hat{S}$	Entropy (W/K)
$T$	Temperature (K)
$u (u, v)$	Velocity components (m/s)
$x (x, y)$	Lattice coordinates (m)

### Subscripts

0	Represents the Newtonian fluid
ff	Fluid friction
HT	Heat transfer
$i$	Lattice direction
mf	Magnetic field
NF	Nanofluid
NP	Nanoparticle
PF	Pure fluid
R	Radiative

### Superscripts

$b$	Repeating variable
eq	Equilibrium

## 1 Introduction

Natural convection heat transfer (NCHT) is one of the most crucial heat transmission methods that does not require any outside forces. Numerous natural phenomena and industrial applications, such as fire dynamics, bioreactor design, solar energy performance, geophysical systems, and crystal

fabrication, have attracted significant experimental, numerical, and theoretical attention due to the NCHT in the confined chamber (Shekaramiz et al. 2021; Malkeson et al. 2023; Nemati et al. 2023; Yuan et al. 2023).

Among the passive methods that provide the possibility of changing the NCHT flow characteristics is adding nanoparticles to a pure fluid and changing the geometry of the chamber. In most real and industrial applications around this phenomenon, the working fluid produces a low heat transfer (HT) rate due to the low coefficient of thermal conductivity. For this reason, it is very useful to add materials that increase the conductivity coefficient (Toghraie et al. 2019; Khodabandeh et al. 2019; Mousavi et al. 2020; Mohebbi and Ma 2023). Nanofluids are new domains that have the potential to be used in engineering, particularly for the creation of the newest bio-medical tools and techniques. Automotive, Nuclear, and electronics applications are some of the industrial uses of nanofluids. In comparison to readily available pure fluids like water and oils, nanofluids not only offer improved thermal characteristics, but also additional advantages like minimal wearing and excellent stability (Alrowaili et al. 2022). Given the importance of the beneficial characteristics of these passive methods, Rashid et al. (2023) inquired the influence of the shape of the nanoparticles on nanofluid flow in a lid-driven square cavity with a fixed circular obstruction in the middle. According to the study, nanoparticles having a lamina (non-spherical) shape perform temperature distribution and heat transfer in diamond-water nanofluid more efficiently. To analyze the naturally convective Cu-water nanofluid flow with an oscillating temperature profile, Saleem et al. (2023) took into account an L-shaped cavity. The research demonstrated that the use of nanofluid and a greater Rayleigh Number (Ra) consistently increased free convection effects. Among other results, the decrease in HT rate was due to the increase in the ratio of the enclosure aspect ratio. They reported that by changing the chamber aspect ratio, it is possible to change the flow characteristics due to the presence of other parameters.

The extensive use of non-Newtonian fluids in practical applications and a variety of sectors, including the chemical industry, is one of the most crucial elements that researchers must consider while examining and evaluating the flow of these fluids. Since viscosity in non-Newtonian fluids solely depends on temperature and pressure, it is independent of outside forces (Zhao et al. 2023; Sulochana et al. 2023; Nemati and Sefid 2023). It is impossible to represent the shear stress state in non-Newtonian fluids using a constant coefficient like viscosity. The flow of blood in the body is one of the most significant and practical non-Newtonian fluids (Eichler et al. 2023; Asha et al. 2023; Tazangi et al. 2021). Loenko et al. (2019) conducted a numerical simulation to investigate the NCHT of a power-law (PL) fluid in a closed cavity with a heat-generating and heat-conducting

element. The study showed that the growth of the PL index slows down the flow and HT in the cavity, and thus, for a shear thinning fluid, heat removal from the energy source occurs more intensively. Almensoury et al. (2021) investigated the NCHT of a non-Newtonian nanofluid inside a F-shaped porous cavity. The study's important findings imply that the inclusion of nanoparticles has a major impact on HT rates.

Various real-world procedures are significantly impacted by thermal radiation when coupled with free convection, including solar collectors, electronic device cooling, high temperature heat exchangers, and industrial furnaces. Many of these applications and processes would greatly benefit from a faster rate of heat transfer through thermal radiation through the fluids (Wahid et al. 2023; Sharma et al. 2023; Jha and Samaila 2023). Tighchi et al. (2019) took into account a square cavity to assess the combined impact of volumetric radiation and free convection via the lattice Boltzmann method (LBM) simulation. They proved that the effect of increasing nanoparticles that increase the Nusselt Number (Nu) value is controlled by the presence of radiation. For the higher Ra values, radiation is more effective in improving the thermal characteristics of the system. The LBM was used by Safaei et al. (2018) to model the interaction of thermal surface radiation and nanofluid free convection in a shallow cavity. The study came to the conclusion that when radiative HT and free convection are combined, the flow field is changed and the mean Nu value is also increased. Radiation is therefore a crucial element in sustaining the rate of HT.

To build energy systems with the best possible efficiency, it is crucial to examine the generation of entropy (GE) as a way to measure workability loss. HT resulting from a small temperature difference, fluid viscosity, and magnetic field (MF) can be mentioned as factors of entropy formation (Zhang et al. 2020; Eid and Mabood 2020; Ijaz et al. 2021; Shehzad et al. 2021). Pordanjani et al. (2019) employed a tilted rectangular chamber to explore the NCHT and GE of nanofluid in the presence of thermal radiation. The analysis demonstrated that upon enhancing the Hartmann Number (Ha), the total entropy formation and HT rate decrease, while the Bejan number (Be) enhances. Nemati and Farahani (2023) developed a model of non-uniform MF with heat absorption/production to determine the amount of GE by conjugate HT of the PL liquid within a K-shaped cavity. According to the study, the influence of augmenting the Ha value on the entropy formation revealed a significant enhancement of about 30% in heat production mode and a reduction of about 10% in heat absorption mode.

Utilizing MF influence on fluid flow is one way to regulate convection-related HT. Magnetohydrodynamics (MHD) is the study of fluid flow subjected to MF. HT and flow characteristics, for instance, may be modified and managed by employing MHD natural convection currents

in fluids (Barnoon et al. 2021; Arulmozhi et al. 2022; Butt et al. 2023; Ali et al. 2022). MHD investigates the interaction of fluid and magnetic force. The MHD NCHT is of great interest to researchers due to its Numerous industrial applications. Mourad et al. (2022) accounted a numerical study of the MHD NCHT and the entropy formation of Cu–water nanofluid in complex geometry. The study showed that due to the direction of MF, applying Lorentz's force reduced the average Nu value; however, this impact was less noticeable for the lower Ra values than at the higher ones. In a square inclined cavity, Pordanjani et al. (2019) accounted a hybrid nanofluid to study the influence of the presence of MF on the rate of the NCHT and entropy formation. The results exhibited that with an increase in the intensity of MF and the length of the thermal source, the total GE improved.

A crucial fundamental subject is the enhancement of HT in complex geometries. This relevance is once again seen in Numerous engineering and industrial fields, such as superheaters, the cooling of electronic devices in limited space, and heat exchangers. The main consideration is managing HT within a variety of gates and intricate shapes. Because of this, numerous numerical and experimental studies on the convection fluid flow inside various cavity geometries have been conducted recently (Aly and Raizah 2020; Mohebbi et al. 2021; Chammam et al. 2021; Zhou et al. 2023). According to the study conducted by Ali et al. (2020), which simulated the impact of an external MF on the hydrothermal aspects of free convection of a PL non-Newtonian nanofluid inside a baffled U-shape enclosure, the HT rate increases as the aspect ratio of the cold rib of the U-profiles rises due to the increased HT area, even though convection effects decrease. By placing a rhombus-shaped object in the path of non-Newtonian fluid flow, Bai et al. (2022) exhibited that there are the highest convection effects when placing the object at a hot temperature. Another result is the change in flow power and thermal characteristics, including entropy and the mean Nu value, by changing the angle of the chamber placement. Also, they proved that the lowest effect of MF presence is visible in the heat absorption mode.

One of the features of the present work is the simultaneous investigation of the effect of thermal radiation and heat absorption in determining the thermal performance index of a hot electronic component in a specific geometry through the NCHT, which has not been investigated so far. Another feature is the comprehensiveness of the analysis of the effect of various parameters, including the imposed MF position, on the system's thermal characteristics via LBM.

The presentation of the governing equations and relationships related to nanofluid modeling along with the necessary details for the numerical solution method is described in the second section. The third section is dedicated to present the analysis of the mesh study along with the validation of

the code written both qualitatively and quantitatively. The fourth section contains the results and analysis of the simulation findings. At the end, a summary of the present work is provided.

## 2 Modeling

### 2.1 Description of the Problem Geometry

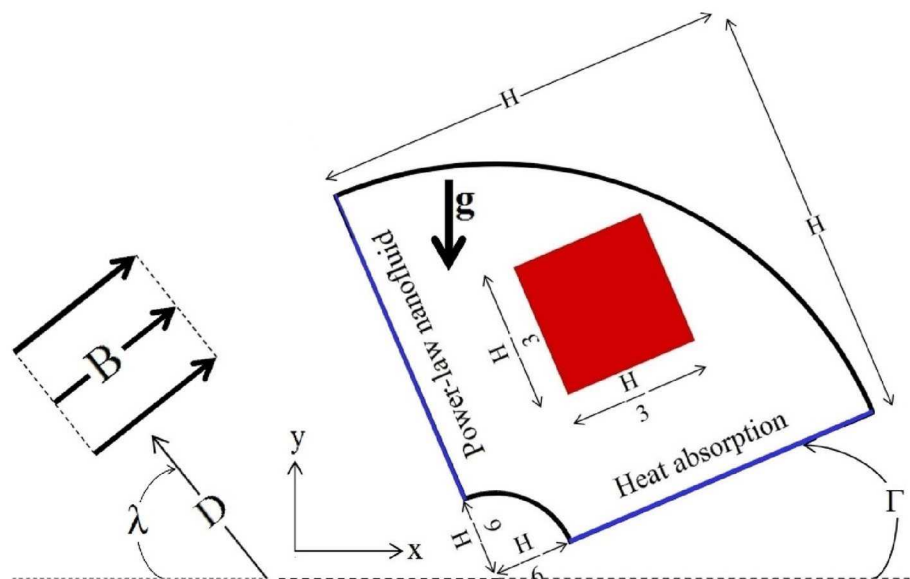
The present work deals with modeling the cooling of a hot electronic component enclosed in a part of a ring filled with the PL nanofluid. The process of reducing the temperature of a hot body is done via the NCHT, which is exposed to thermal radiation and uniform heat absorption. The fluid is assumed to be as a radiatively active environment, so the existing fluid is assumed to be homogeneous, gray, and participating in isotropic absorption, diffusion, and scattering. The uniform MF is imposed on the flow inside the chamber under the angle  $\lambda$  at different locations with  $D$  index ( $D1 = 0$ ,  $D2 = \frac{H}{3}$ ,  $D3 = \frac{2H}{3}$ ). In Table 1, the position of applying MF is presented according to the angle of application. There are two reasons for considering the variable position of applying MF: (a) the existence of

**Table 1** The position of applying MF according to the application angle

	$\lambda=0$	$\lambda=90^\circ$
D1	$B = B_M; \frac{2H}{3} < x \leq H$	$B = B_{MAX}; 0 \leq y \leq \frac{H}{3}$
D2	$B = B_M; \frac{H}{3} < x \leq \frac{2H}{3}$	$B = B_{MAX}; \frac{H}{3} < y \leq \frac{2H}{3}$
D3	$B = B_M; 0 \leq x \leq \frac{H}{3}$	$B = B_{MAX}; \frac{2H}{3} < y \leq H$

$B_M$  represents the highest imposed MF strength

**Fig. 1** The geometry of the problem under investigation



such conditions in reality, and (b) achieving specific results by not exerting MF throughout the chamber. The chamber is rotated under at an angle  $\Gamma$  relative to the horizon so that the curved walls are adiabatic. The two cavity smooth walls are at a constant cold temperature. The coordinates of the center of the hot body are  $(\frac{H}{2}, \frac{H}{2})$ . For the radiation boundary conditions in this study, it is assumed that the reflection and emission of radiation from the walls are completely diffused in all directions with a diffusion coefficient of  $\epsilon=1$ . The geometry of the current study is depicted in Fig. 1.

The assumptions included during the simulation are presented in Table 2. The characteristics of nanoparticles suspended in the main fluid are shown in Table 3 (Zainodin et al. 2023 and Kamis et al. 2023).

### 2.2 Governing Equations

Nanofluid modeling is done through Eqs. (1)–(7) (Selimefendigil and Chamkha 2019; Wang et al. 2019; Chen and Shu 2020). In determining the nanofluid thermal conductivity coefficient related to Eq. (7), the coefficient of  $m$  refers to the nanoparticle shape factor. The values of this parameter are provided in Table 4 (Chamkha et al. 2018; Dogonchi et al. 2019).

$$\mu_{NF} = \frac{\mu_{PF}}{(1 - \varphi_{NP})^{-2.5}} |\gamma|^{(n-1)} \quad (1)$$

$$\rho_{NF} = [\rho\varphi]_{NP} + \rho_{PF}(1 - \varphi_{NP}) \quad (2)$$

$$\frac{(C_p)_{NF}}{(C_p)_{PF}} = \left[ \frac{1}{1 + \frac{(1-\varphi_{NP})}{\varphi_{NP}\rho_{NP}}} \frac{(C_p)_{NP}}{(C_p)_{PF}} + \frac{1}{1 + \frac{\varphi_{NP}\rho_{NP}}{(1-\varphi_{NP})}} \right] \quad (3)$$

**Table 2** Simulation assumptions

(1)	The 2D flow is considered steady state and laminar
(2)	The power-law non-Newtonian fluid is incompressible
(3)	Except for the density that follows the Boussinesq approximation, the rest of the properties are constant
(4)	There is no slip and fluid penetration on the surfaces
(5)	Nanoparticles suspended in the pure fluid form a single phase composition
(6)	The nanoparticles and pure fluid are in thermal equilibrium
(7)	Viscous loss is neglected, and radiation effects are considered as volumetric force in the energy equation

**Table 3** The nanoparticles/pure fluid thermophysical properties

Symbol	Unit	H <sub>2</sub> O	Fe <sub>3</sub> O <sub>4</sub>
Pr	–	6.23	–
σ	(Ω.m)	0.05	25,000
β	(1/K)	21 × 10 <sup>-5</sup>	1.3 × 10 <sup>-5</sup>
C <sub>p</sub>	(J/kg K)	4179	670
k	(W/m K)	0.613	6
ρ	(kg/m)	997.1	5200

**Table 4** Values related to nanoparticles shape

Particle shape	Spherical	Cylindrical	Platelet	Column	Lamina
<i>m</i>	3	4.8	5.7	6.37	16.16

$$\frac{(\beta)_{NF}}{(\beta)_{PF}} = \left[ \frac{1}{1 + \frac{(1-\varphi_{NP})}{\varphi_{NP}\rho_{NP}}} \frac{\beta_{NP}}{\beta_{PF}} + \frac{1}{1 + \frac{\varphi_{NP}\rho_{NP}}{(1-\varphi_{NP})}} \right] \quad (4)$$

$$\alpha_{NF} = \frac{k_{NF}}{(\rho C_p)_{NF}} \quad (5)$$

$$\frac{\sigma_{NF}}{\sigma_{PF}} = \left[ 1 + \frac{3\varphi_{NP} \left( \frac{\sigma_{NP}}{\sigma_{PF}} - 1 \right)}{\left( \frac{\sigma_{NP}}{\sigma_{PF}} + 1 \right) - \varphi_{NP} \left( \frac{\sigma_{NP}}{\sigma_{PF}} - 1 \right)} \right] \quad (6)$$

$$\frac{k_{NF}}{k_{PF}} = \left[ \frac{(m-1)(k_{NP} + k_{PF}) + (1-m)\varphi_{NP}(k_{PF} - k_{NP})}{\varphi_{NP}(k_{NP} + k_{PF}) + k_{NP} + (m-1)k_{PF}} \right] \quad (7)$$

The governing equations in dimensional form for solving the problem are presented in Eqs. (8)–(13).

$$\frac{\partial u}{\partial x} + \frac{\partial v}{\partial y} = 0 \quad (8)$$

$$u \frac{\partial u}{\partial x} + v \frac{\partial u}{\partial y} = \frac{-\frac{\partial p}{\partial x} + \left( \frac{\partial \tau_{xx}}{\partial x} + \frac{\partial \tau_{xy}}{\partial y} \right)}{\rho_{NF}} + \frac{g(\rho\beta)_{NF}(T - T_{cold}) \sin \Gamma + \sigma_{NF} B^2 (v \sin \lambda \cos \lambda - u \cos^2 \lambda)}{\rho_{NF}} \quad (9)$$

$$u \frac{\partial v}{\partial x} + v \frac{\partial v}{\partial y} = \frac{-\frac{\partial p}{\partial y} + \left( \frac{\partial \tau_{xy}}{\partial x} + \frac{\partial \tau_{yy}}{\partial y} \right)}{\rho_{NF}} + \frac{g(\rho\beta)_{NF}(T - T_{cold}) \cos \Gamma + B^2 \sigma_{NF} (u \sin \lambda \cos \lambda - v \sin^2 \lambda)}{\rho_{NF}} \quad (10)$$

$$\tau_{ij} = \mu_{NF} \left( \frac{\partial u_i}{\partial x_j} + \frac{\partial u_j}{\partial x_i} \right) \quad (11)$$

$$\mu_{NF} = \left\{ 2 \left[ \left( \frac{\partial u}{\partial x} \right)^2 + \left( \frac{\partial v}{\partial y} \right)^2 \right] + \left( \frac{\partial v}{\partial x} + \frac{\partial u}{\partial y} \right)^2 \right\}^{\frac{(n-1)}{2}} \quad (12)$$

$$u \frac{\partial T}{\partial x} + v \frac{\partial T}{\partial y} = \alpha_{NF} \left[ \frac{\partial^2 T}{\partial x^2} + \frac{\partial^2 T}{\partial y^2} + \frac{q}{(\rho C_p)_{NF}} \right] - \frac{1}{(\rho C_p)_{NF}} \frac{\partial \dot{q}_R}{\partial y} \quad (13)$$

The amount of entropy formed due to the presence of imposed MF, HT and fluid friction is presented in relations (14)–(16), respectively. The total GE value has also appeared in Eq. (17) (Khan et al. 2022; Rahman et al. 2021; Kashyap et al. 2021).

$$\hat{S}_{mf}^{\lambda=90^\circ} = \frac{B^2 \sigma_{NF}}{T_{hot} + T_{cold}} v^2 \quad \text{and} \quad \hat{S}_{mf}^{\lambda=0} = \frac{B^2 \sigma_{NF}}{T_{hot} + T_{cold}} u^2 \quad (14)$$

$$\hat{S}_{ht} = \frac{k_{NF}}{\left( \frac{T_{hot} + T_{cold}}{2} \right)^2} \left[ \left( \frac{\partial T}{\partial x} \right)^2 + \left( \frac{\partial T}{\partial y} \right)^2 \right] \quad (15)$$

$$\hat{S}_{ff} = \frac{\mu_{NF}}{\frac{T_{hot} + T_{cold}}{2}} \left[ 2 \left( \left( \frac{\partial u}{\partial x} \right)^2 + \left( \frac{\partial v}{\partial y} \right)^2 \right) + \left( \frac{\partial u}{\partial y} + \frac{\partial v}{\partial x} \right)^2 \right] \quad (16)$$

$$\hat{S} = \hat{S}_{ff} + \hat{S}_{ht} + \hat{S}_{mf} \quad (17)$$

In non-Newtonian fluid modeling, the shear rate is different at each node, and the viscosity does not have a constant value. Considering that the non-Newtonian fluid is approximated by the PL model in the available study, the computation of the kinematic viscosity in terms of the shear rate in the nodes is according to Eq. (18) (Mohebbiet al. 2019; Mendu and Das 2021; Dong et al. 2018).

$$v(x, t) = v_0 |\gamma| = \left( \sqrt{2 \times 0.5 \left( \frac{\partial u_i}{\partial x_j} + \frac{\partial u_j}{\partial x_i} \right) \times 0.5 \left( \frac{\partial u_i}{\partial x_j} + \frac{\partial u_j}{\partial x_i} \right)} \right)^{(n-1)} \quad (18)$$

By introducing dimensionless parameters in Eq. (19), the governing equations and the determining equations of GE are written in dimensionless form as relations (20)–(28).

$$\begin{aligned} Ra &= \frac{\beta \theta g H^{2n+1}}{v_0 \alpha^n}, P = \frac{\rho H^2}{\rho Ra \alpha^2}, Pr = \frac{\nu}{\alpha}, RP = \frac{4T_C^3 \sigma_R}{\beta_R k_{PF}}, X = \frac{x}{H}, Y = \frac{y}{H}, \\ U &= \frac{uH}{\alpha \sqrt{Ra}}, V = \frac{vH}{\alpha \sqrt{Ra}}, v_0 = \frac{\mu_0}{\rho}, Pr = \frac{\nu_0 H^{2-n}}{\alpha^{2-n}}, \Delta = \frac{H^2 q}{(\rho C_p)_{NF} \alpha_{PF}}, \\ Ha &= BH^n \sqrt{\frac{\sigma_{NF} \alpha^{1-n}}{\mu_{PF}}}, \theta = \frac{T - T_{cold}}{T_{hot} - T_{cold}}, S = \hat{S} \frac{\left( \frac{T_{hot} + T_{cold}}{2} \right)^2 H^2}{k_{BF} (T_{hot} - T_{cold})^2} \end{aligned} \quad (19)$$

$$\frac{\partial U}{\partial X} + \frac{\partial V}{\partial Y} = 0 \quad (20)$$

$$S_{ht} = \frac{k_{NF}}{\left( \frac{T_{hot} + T_{cold}}{2} \right)^2} \left[ \left( \frac{\partial \theta}{\partial X} \right)^2 + \left( \frac{\partial \theta}{\partial Y} \right)^2 \right] \quad (25)$$

$$S_{ff} = A^* k_{NF} \left[ 2 \left( \frac{\partial U}{\partial X} \right)^2 + 2 \left( \frac{\partial V}{\partial Y} \right)^2 + \left( \frac{\partial U}{\partial X} + \frac{\partial V}{\partial Y} \right)^2 \right] \quad (26)$$

$$A^* = \frac{\left( \frac{T_{hot} + T_{cold}}{2} \right)}{k_{PF}} \left( \frac{H}{T_{hot} - T_{cold}} \right) \quad (27)$$

$$S = S_{ff} + S_{ht} + S_{mf} \quad (28)$$

To determine the power of the flow, the stream function is defined in the form of Eq. (29).

It should be noted that the total GE amount and the Be value (the ratio of the amount of GE caused by HT to the

$$\begin{aligned} U \frac{\partial U}{\partial X} + V \frac{\partial U}{\partial Y} &= -\frac{\partial P}{\partial X} + Pr \left[ \frac{\rho_f \mu_{NF}}{\rho_{NF} \mu_f} \right] \left( \frac{\partial^2 U}{\partial Y^2} + \frac{\partial^2 U}{\partial X^2} \right) \\ &\quad - Pr Ha^2 \left[ \frac{\rho_f \mu_{NF}}{\rho_{NF} \mu_f} \right] (V \sin \lambda \cos \lambda - U \cos^2 \lambda) + Ra Pr \left[ \frac{\beta_{NF}}{\beta_f} \right] \theta \sin \Gamma \end{aligned} \quad (21)$$

$$\begin{aligned} U \frac{\partial V}{\partial X} + V \frac{\partial V}{\partial Y} &= -\frac{\partial P}{\partial Y} + Pr \left[ \frac{\rho_f \mu_{NF}}{\rho_{NF} \mu_f} \right] \left( \frac{\partial^2 V}{\partial Y^2} + \frac{\partial^2 V}{\partial X^2} \right) \\ &\quad - Pr Ha^2 \left[ \frac{\rho_f \mu_{NF}}{\rho_{NF} \mu_f} \right] (U \sin \lambda \cos \lambda - V \cos^2 \lambda) + Ra Pr \left[ \frac{\beta_{NF}}{\beta_f} \right] \theta \cos \Gamma \end{aligned} \quad (22)$$

$$U \frac{\partial \theta}{\partial X} + V \frac{\partial \theta}{\partial Y} = \frac{\alpha_{NF}}{\alpha_{PF}} \left[ \left( \frac{\partial^2 \theta}{\partial X^2} + \frac{\partial^2 \theta}{\partial Y^2} \right) + q\theta + \frac{4}{3} RP \left[ \left( \frac{k_{NF}}{k_f} \right)^{-1} \frac{(\rho C_p)_f k_{NF}}{(\rho C_p)_{NF} k_f} \frac{\partial^2 \theta}{\partial Y^2} \right] \right] \quad (23)$$

$$S_{mf}^{\lambda=90^\circ} = \chi \frac{Ha^2 \sigma_{NF}}{\sigma_{PF}} V^2 \text{ and } \hat{S}_{mf}^{\lambda=0} = \chi \frac{Ha^2 \sigma_{NF}}{\sigma_{PF}} U^2 \quad (24)$$

total GE) are expressed in an averaged form according to Eqs. (30) and (31) (Khan et al. 2022; Rahman et al. 2021; Kashyap et al. 2021). The value of the mean Nu is calculated as the sum of the values on the enclosure cold walls according to Eq. (32).

It is necessary to explain that Eq. (33) indicates the ratio of the mean Nu value to the total GE value under the name of the system thermal performance index (TPI).

$$U = \frac{\partial \Psi}{\partial Y} \text{ and } V = -\frac{\partial \Psi}{\partial X} \tag{29}$$

$$S = \int_0^1 \int_0^1 S dXdY = \int_0^1 \int_0^1 [S_{ff} + S_{ht} + S_{mf}] dXdY \tag{30}$$

$$Be = \int_0^1 \int_0^1 \frac{S_{ht}}{[S_{ff} + S_{ht} + S_{mf}]} dXdY \tag{31}$$

$$Nu = Nu_{\text{Vertical}} = \frac{1}{5H} \int_0^H \frac{k_{NF}}{k_{PF}} \left( \frac{\partial \theta}{\partial X} \right)_{X=0} dY + Nu_{\text{Horizontal}} = \frac{1}{5H} \int_0^H \frac{k_{NF}}{k_{PF}} \left( \frac{\partial \theta}{\partial Y} \right)_{Y=0} dX \tag{32}$$

$$\zeta = \frac{Nu}{S} \tag{33}$$

### 2.3 Numerical Method

One of the computational fluid flow analysis techniques that has achieved remarkable success in resolving different HT issues is the lattice Boltzmann method, often known as LBM. The primary concept is founded in the theory of kinetic energy of particles in order to examine the motion and collision of particles in this mesoscopic approach. The lattice Boltzmann equation is a simple evolution equation for the particle distribution function that expresses the likelihood of finding particles at a given position and velocity on the grid during a given period of time. It is the

creator of the Boltzmann evolution equations for special distribution functions. The main equation of LBM, for calculating the density and fields of velocity with the external force term, is expressed as Eq. (34) (Kebriti and Moqtaderi 2021; Rahman et al. 2022; Islam et al. 2023). In the present work, the  $D_2Q_9$  network arrangement is used for modeling. A view of the arrangement of this type of lattice is depicted in Fig. 2a. The equilibrium distribution function, the discretized network velocities, and the relaxation time related to the flow field are presented in Eqs. (35) to (37), respectively (Mohebbi et al. 2021).

$$f_i(\mathbf{x} + \mathbf{c}_i, t + 1) = f_i(\mathbf{x}, t) + \frac{[f_i^{\text{eq}}(\mathbf{x}, t) - (f_i(\mathbf{x}, t))] }{\tau_f} + \mathbf{F}_i \mathbf{c}_i \tag{34}$$

$$f_i^{\text{eq}} = \omega_i \left[ 1 + 3(\mathbf{c}_i \cdot \mathbf{u}) + \frac{9}{2}(\mathbf{u} \cdot \mathbf{u}) - \frac{3}{2}(\mathbf{c}_i \cdot \mathbf{u})^2 \right] \tag{35}$$

$$\mathbf{c}_i = \begin{pmatrix} c_{ix} \\ c_{iy} \end{pmatrix} = \begin{pmatrix} 0 & 1 & 0 & -1 & 0 & -1 & 1 & -1 & 1 \\ 0 & 0 & 1 & 0 & -1 & 1 & 1 & -1 & -1 \end{pmatrix} \tag{36}$$

$$\tau_f = (3v(x, t) + 0.5) \tag{37}$$

The weighting coefficients are presented in the form of Eq. (38), and kinematic viscosity is provided in the form of Eq. (39) (Kashyap et al. 2021).

$$\omega_0 = \frac{4}{9}, \omega_{1-4} = \frac{1}{9}, \omega_{5-8} = \frac{1}{36} \tag{38}$$

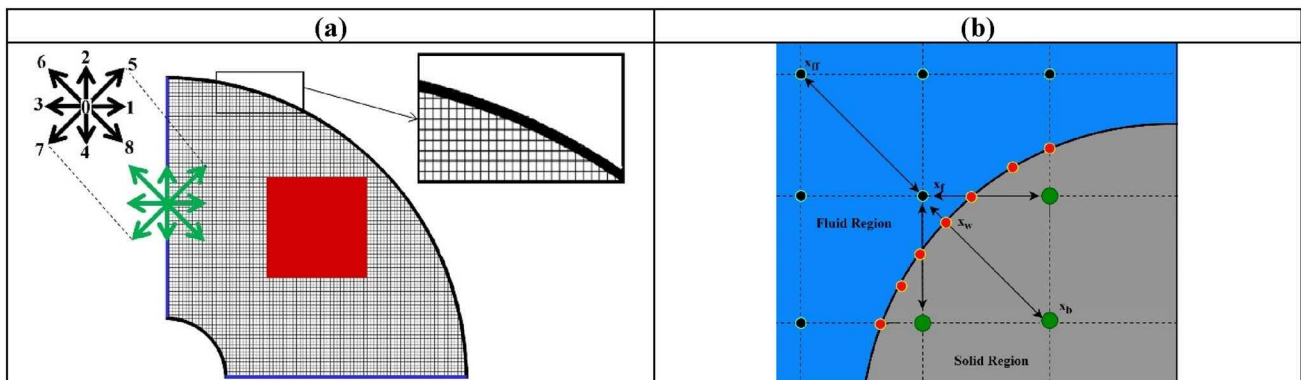


Fig. 2 a The  $D_2Q_9$  network arrangement in computational domain and b a representation of the curved boundary

$$v(\mathbf{x}, t) = v_0 |\gamma|^{(n-1)} \tag{39}$$

The shear rate in the nodes is obtained in LBM according to Eq. (40) (Mohebbi et al. 2021). The external force in relation (36) is added to the Boltzmann equation according to Eq. (41) (Mendu and Das 2021).

$$\gamma_{ij} = -\frac{3}{2\tau_f \rho c^2} \sum_{i=0}^8 c_{ix} c_{iy} (f_i - f_i^{eq}) \tag{40}$$

$$\begin{aligned} \mathbf{F}_i &= \mathbf{F}_x + \mathbf{F}_y, \\ \mathbf{F}_x &= 3\omega_i \rho_{PF} Ha^2 \left( \frac{\mu_{NF}}{H^2} \right) [v \sin \lambda \cos \lambda - u \cos^2 \lambda], \\ \mathbf{F}_y &= 3\omega_i g(\rho\beta)_{NF} \theta + 3\omega_i \rho_{PF} Ha^2 \left( \frac{\mu_{NF}}{H^2} \right) [u \sin \lambda \cos \lambda - v \sin^2 \lambda] \end{aligned} \tag{41}$$

Similar to the flow field, an equation is written for the temperature field in the form of Eq. (42) where  $h$  is the distribution function of the temperature field. To model thermal radiation, volumetric force is added as a source term, and to show the effect of heat absorption/production, a term containing the power of this phenomenon is added to the temperature field equation. In the energy equation of relation (42), the first term and the second term on the right side of the equation represent the source terms for the existence of heat absorption/generation and radiation flux divergence, respectively. The equilibrium distribution function and the relaxation time factor related to the temperature field are presented in Eqs. (43) and (44), respectively (Safaei et al. 2018; Tighchi et al. 2019; Zhang et al. 2020).

$$h_i(\mathbf{x}+\mathbf{c}_i, t+1) - h_i(\mathbf{x}, t) + \frac{[h_i(\mathbf{x}, t) - h_i^{eq}(\mathbf{x}, t)]}{\tau_h} = \frac{q}{(\rho C_p)_{NF}} (T - T_c) - \frac{\omega_i}{(\rho C_p)_{NF}} \nabla \cdot \vec{q}_R \tag{42}$$

$$\begin{cases} h_0^{eq} = -\omega_i T [1 + 3(\mathbf{c}_i \cdot \mathbf{u})] \\ h_{1-4}^{eq} = \omega_i T \left[ \frac{3}{2} + \frac{3}{2}(\mathbf{c}_i \cdot \mathbf{u}) + \frac{9}{4}(\mathbf{c}_i \cdot \mathbf{u})^2 - \frac{3}{2}(\mathbf{u} \cdot \mathbf{u}) \right]; 1 \leq i \leq 4 \\ h_{5-8}^{eq} = \omega_i T \left[ 3 + 6(\mathbf{c}_i \cdot \mathbf{u}) + \frac{9}{2}(\mathbf{c}_i \cdot \mathbf{u})^2 - \frac{3}{2}(\mathbf{u} \cdot \mathbf{u}) \right]; 5 \leq i \leq 8 \end{cases} \tag{43}$$

$$\tau_h = (3\alpha(\mathbf{x}, t) + 0.5) \tag{44}$$

The existence of the participating medium (absorbing, reflecting, and scattering) for radiation rays makes the heat transfer of radiation a volumetric phenomenon, and for its analysis, volumetric methods such as LBM are used. All problems in which there is heat transfer are affected by radiation heat transfer, but according to the temperature, this effect can be high or low (Tighchi et al. 2018).

The radiation flux divergence in relation (42) is expressed according to Eq. (45) (Sobhani et al. 2018).

The radiative transfer equation in each  $S_R$  direction is expressed according to Eq. (46). In this regard,  $I$  represent the radiation intensity (Sobhani et al. 2018).

$$\begin{aligned} \vec{q}_R &= -\frac{4}{3} \frac{\sigma_R}{\beta_R} \frac{\partial T^4}{\partial y}, T^4 = 4T_c^3 T - 3T_c^4 \\ \nabla \cdot \vec{q}_R &= \beta_R (1 - \omega_R) (4\pi I_b - G) \end{aligned} \tag{45}$$

$$\frac{dI}{dS_R} = -\beta_R I + \beta_R (1 - \omega_R) + \frac{T^4 \sigma_R}{4} + \frac{\beta_R \omega_R}{4\pi} G \tag{46}$$

Assuming the local radiative balance ( $G = 4\pi I_b$ ), so that  $I_b$  is equal to  $\frac{4T^4}{\pi}$ , Eq. (48) can be converted into Eq. (47) (Sobhani et al. 2018).

$$\frac{dI}{dS_R} = -\beta_R I + \frac{\beta_R}{4\pi} G \tag{47}$$

After a series of discretization calculations, Eq. (48) can be expressed according to Eq. (48) (Tighchi et al. 2018).

$$I_i(\mathbf{x} + \mathbf{c}_i, t + 1) = I_i(\mathbf{x}, t) - \frac{1}{\tau_R} [I_i(\mathbf{x}, t) - I_i^{eq}(\mathbf{x}, t)] \tag{48}$$

In the above relation,  $\tau_R$  represents the radiation relaxation time coefficient and is written according to relation (49). The radiation equilibrium distribution function is also expressed according to Eq. (50) (Tighchi et al. 2018).

$$\tau_R = \frac{1}{\beta_R c_i} \tag{49}$$

$$I_i^{eq} = \sum_{i=1}^8 I_i \tag{50}$$

In this study, calculations have been done for  $\omega_R = \frac{\sigma_R}{\beta_R}$  and  $\omega_R = 0.1$ . Finally, the macroscopic quantities, including density, velocity, and temperature, are calculated using distribution functions according to Eq. (51) (Rezaie and Norouzi 2018).

$$\rho = \sum_{i=0}^8 f_i, \mathbf{u} = \frac{\sum_{i=0}^8 \mathbf{c}_i f_i}{\rho}, T = \sum_{i=0}^8 h_i \tag{51}$$

In the presented relationships, the superscript (eq) refers to the equilibrium variable.

To exert the boundary conditions on the smooth walls, the bounce back model according to references (Mohebbi et al. 2019; Chen and Shu 2020; Asha et al. 2023) was used. In this model, the unknown distribution functions entered into the domain are designated based on the known distribution functions outside of the computational scope. The boundary conditions on the cavity vertical cold wall are in accordance with Eq. (52), while the boundary conditions on the cavity horizontal cold wall are in the form of Eq. (53).

definition of a kind of virtual distribution function for the nodes near the border of the curve. In this method, according to Fig. 2b, based on the location of the boundary node  $w$  between two nodes  $b$  and  $f$ , the variable  $\Delta_{\text{curved}}$  is defined as  $\Delta_{\text{curved}} = \left| \frac{x_f - x_w}{x_f - x_b} \right|$ . Subscript  $w$ : indicator of the intersection of the curved boundary with the Cartesian lattice, subscript  $b$ : the nodes in the solid region, and subscripts  $f$  and  $ff$ : the first and second nodes in each of the directions of the grid within the computational domain.

The virtual distribution function for point  $b$  in  $\vec{\alpha}$  direction

$$\text{Smooth vertical wall} \left\{ \begin{array}{l} \text{Boundary conditions in macroscopic form: } U = V = \theta = \Psi = 0 \\ \text{Boundary conditions in LBM : } \begin{cases} f(1, 0, j) = f(3, 0, j) \\ f(5, 0, j) = f(7, 0, j) \\ f(8, 0, j) = f(6, 0, j) \\ h(1, 0, j) = -h(3, 0, j) \\ h(5, 0, j) = -h(7, 0, j) \\ h(8, 0, j) = -h(6, 0, j) \end{cases} \end{array} \right. \quad (52)$$

$$\text{Smooth horizontal wall} \left\{ \begin{array}{l} \text{Boundary conditions in macroscopic form : } U = V = \theta = \Psi = 0 \\ \text{Boundary conditions in LBM : } \begin{cases} f(2, i, 0) = f(4, i, 0) \\ f(5, i, 0) = f(7, i, 0) \\ f(6, i, 0) = f(8, i, 0) \\ h(2, i, 0) = -h(4, i, 0) \\ h(5, i, 0) = -h(7, i, 0) \\ h(6, i, 0) = -h(8, i, 0) \end{cases} \end{array} \right. \quad (53)$$

Due to the definition of LBM in the Cartesian grid, modeling the curved boundary with this method has always been associated with complications. The bounce back model, despite its simplicity, had a lot of error due to consideration of the curved boundary as a bridge, especially at the high Ra values. That is why other methods have been proposed. Filipova and Hänel (1998) presented the first boundary condition model with second-order accuracy in order to simulate the curved boundary. This method is actually based on the

(perpendicular to a curved surface), based on linear interpolation, is calculated regarding the following equation:

$$\tilde{f}_{\vec{\alpha}}(\vec{x}_b, t) = (1 - \chi)\tilde{f}_{\vec{\alpha}}(\vec{x}_f, t) + \chi f_{\vec{\alpha}}^*(\vec{x}_b, t) - \frac{3}{c^2} 2\rho\omega_{\vec{\alpha}}(\vec{x}_f, t)\vec{c}_{\vec{\alpha}} \cdot \vec{u}_w \quad (54)$$

$$f_{\vec{\alpha}}^*(\vec{x}_b, t) = f_{\vec{\alpha}}^{\text{eq}}(\vec{x}_f, t) + \rho\omega_{\vec{\alpha}}(\vec{x}_f, t)\frac{3}{c^2}\vec{c}_{\vec{\alpha}} \cdot (\vec{u}_{bf} - \vec{u}_f) \quad (55)$$

As suggested by (Mei et al. 1999), Eq. (56) is used to calculate  $\chi$  and  $\vec{u}_{bf}$ .

$$\left\{ \begin{array}{l} \text{if } 0 \leq \Delta_{\text{curved}} < 0.5 \rightarrow \vec{u}_{bf} = \vec{u}_{ff} = \vec{u}(\vec{x}_{ff}, t), \chi = \frac{2\Delta_{\text{curved}} - 1}{(3v + 0.5) - 1} \\ \text{if } 0.5 \leq \Delta_{\text{curved}} \leq 1 \rightarrow \vec{u}_{bf} = \vec{u}_f + \frac{3}{2\Delta_{\text{curved}}}(\vec{u}_w - \vec{u}_f), \chi = \frac{2\Delta_{\text{curved}} - 1}{(3v + 0.5) - 0.5} \end{array} \right. \quad (56)$$

In above equations,  $\vec{c}_\alpha = -\vec{c}_\alpha$ . To apply the temperature boundary conditions accurately, the method recommended by (Guo et al. 2002) is used.

$$\tilde{h}_\alpha(\vec{x}_b, t) = \tilde{h}_\alpha^{eq}(\vec{x}_b, t) + (1 - \frac{1}{(3\alpha + 0.5)})h_\alpha^{neq}(\vec{x}_b, t) \tag{57}$$

$$h_\alpha^{eq}(\vec{x}_b, t) = \omega_\alpha T_b^*(\vec{x}_b, t)[1 + \frac{3}{c_\alpha^2}(\vec{c}_\alpha \cdot \vec{u}_b^*)] \tag{58}$$

$$h_\alpha^{neq}(\vec{x}_b, t) = \Delta_{curved} h_\alpha^{neq}(\vec{x}_f, t)(1 - \Delta_{curved})h_\alpha^{neq}(\vec{x}_{ff}, t) \tag{59}$$

The two parameters  $\vec{u}_b^*$  and  $T_b^*$  are determined according to the following relations depending on the  $\Delta_{curved}$  value (Filippova and Hänel 1998).

$$\begin{cases} \text{if } \Delta_{curved} > 0.75 \rightarrow \vec{u}_b^* = \vec{u}_{b1} \\ \text{if } \Delta_{curved} \leq 0.75 \rightarrow \vec{u}_b^* = \vec{u}_{b1} + (1 - \Delta_{curved})\vec{u}_{b2} \end{cases} \tag{60}$$

$$\begin{cases} \text{if } \Delta_{curved} > 0.75 \rightarrow T_b^* = T_{b1} \\ \text{if } \Delta_{curved} \leq 0.75 \rightarrow T_b^* = T_{b1} + (1 - \Delta_{curved})T_{b2} \end{cases} \tag{61}$$

$$\vec{u}_{b1} = \frac{1}{\Delta_{curved}}[\vec{u}_w + (\Delta_{curved} - 1)\vec{u}_f] \tag{62}$$

$$\vec{u}_{b2} = \frac{1}{(1 + \Delta_{curved})}[2\vec{u}_w + (\Delta_{curved} - 1)\vec{u}_{ff}] \tag{63}$$

$$T_{b1} = \frac{1}{\Delta_{curved}}[T_w(\Delta_{curved} - 1)T_f] \tag{64}$$

$$T_{b2} = \frac{1}{(1 + \Delta_{curved})}[2T_w(\Delta_{curved} - 1)T_{ff}] \tag{65}$$

The present research was done by writing computer code in the Fortran programming language using Microsoft Developer Studio. Calculations were made on a computer with 64 GB of RAM memory and an Intel CORE i7 processor. The calculations continued until the convergence criterion was established. The convergence criterion is expressed according to Eq. (50). The diagrams, figures, and patterns of the flow are drawn through the use of Tecplot EX 2022 R2 software.

### 3 Simulation Sensitivity

It is obligatory to highlight that the criteria for completing the computation to deduct the calculation cost and attain proper accuracy are according to Eq. (66). Index b represents the solution step.

$$\text{Convergence index} : \frac{Nu^{b+1} - Nu^b}{Nu^b} \leq 10^{-5} \tag{66}$$

To exhibit the results independence from the elected lattice, the mean Nu values for different lattice sizes in different cases are presented in Fig. 3a. In addition to the average Nu value, the changes in horizontal velocity for the variations in the dimensions of the network are available in Fig. 3b. Due to the trivial difference between the values associated with 150x150 lattice and 180x180 lattice, the grid with 150x150 dimensions was elected for simulation.

The written code is descriptively checked with the study of (Ilis et al. 2008) to match the results about entropy in

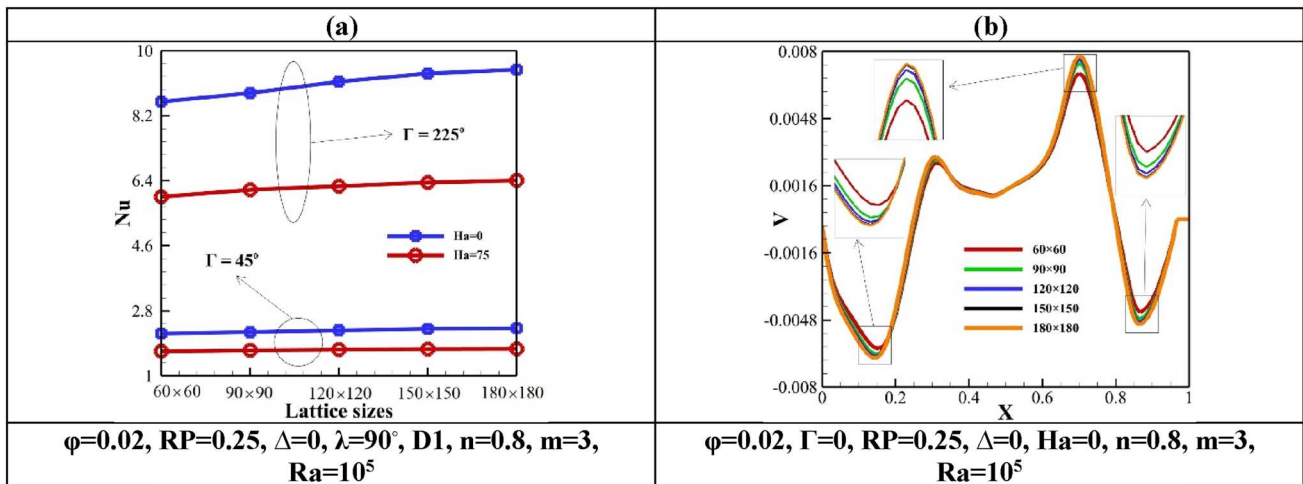


Fig. 3 Checking the independence of the results from the elected lattice

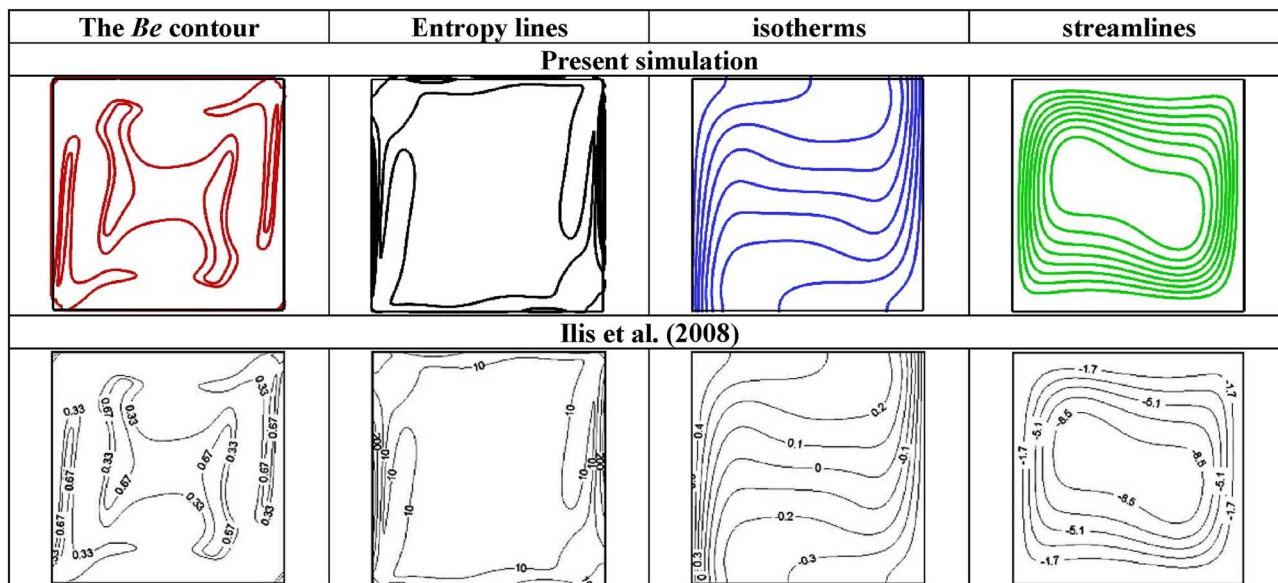


Fig. 4 Comparison of the present results and the study of Ellis et al. (2008)

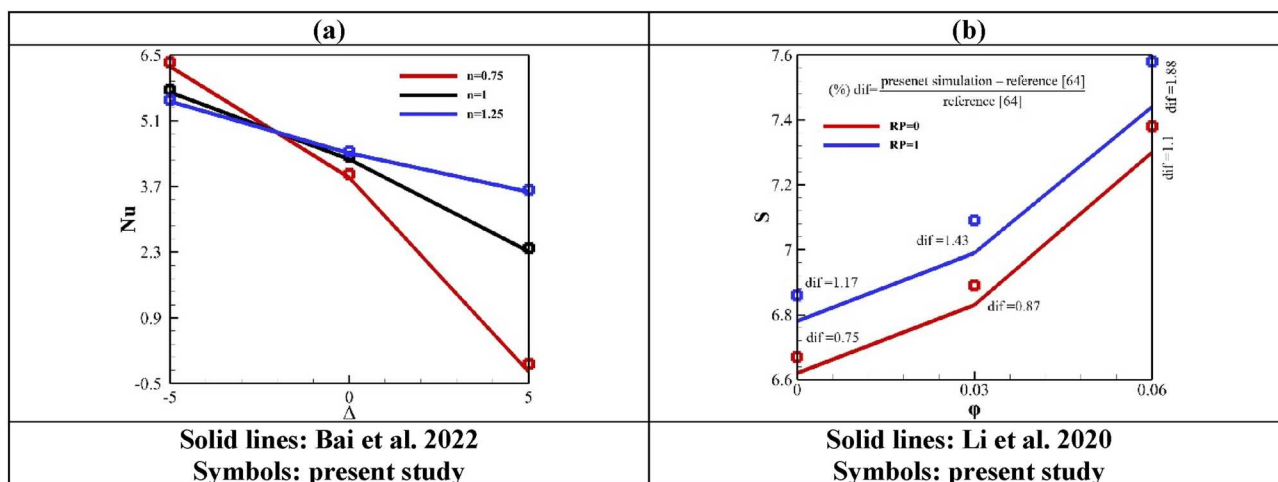


Fig. 5 Comparison of the present results and different references

Fig. 4. In this test case, the NCHT for  $Ra = 10^5$  occurs inside a chamber in the form of a square with non-isothermal walls. The NCHT modeling under the impact of fluid PL index changes within a quarter circle chamber containing a hot body in the presence of heat absorption/generation is compared between the available research and the study conducted by (Bai et al. 2022) in Fig. 5a for  $Ha = 15$  and  $Ra = 10^5$ . Also, a comparison between the available research and study of (Li et al. 2020) regarding the NCHT inside a 2D square chamber filled with nanofluid containing a hot circular body under the effect of radiation and a tilted MF at  $Ha = 20$  and  $Ra = 10^5$  is depicted in Fig. 5b. Considering the limited difference between the results of the present

simulation and reliable references, it is doable to certify the correctness of the performed simulation.

### 4 Results

The purpose of presenting Fig. 6 for  $n = 1$  is to reveal that by changing the cavity inclination angle, in addition to change the shape of the streamlines, the flow power also varies significantly. For  $\Gamma = 45^\circ$  and  $\Gamma = 225^\circ$  at  $Ha = 0$ , because the gravity field affects the chamber symmetrically, the formed vortices (all flow patterns) are completely symmetrical on both sides of the chamber. At these two angles, the fluid

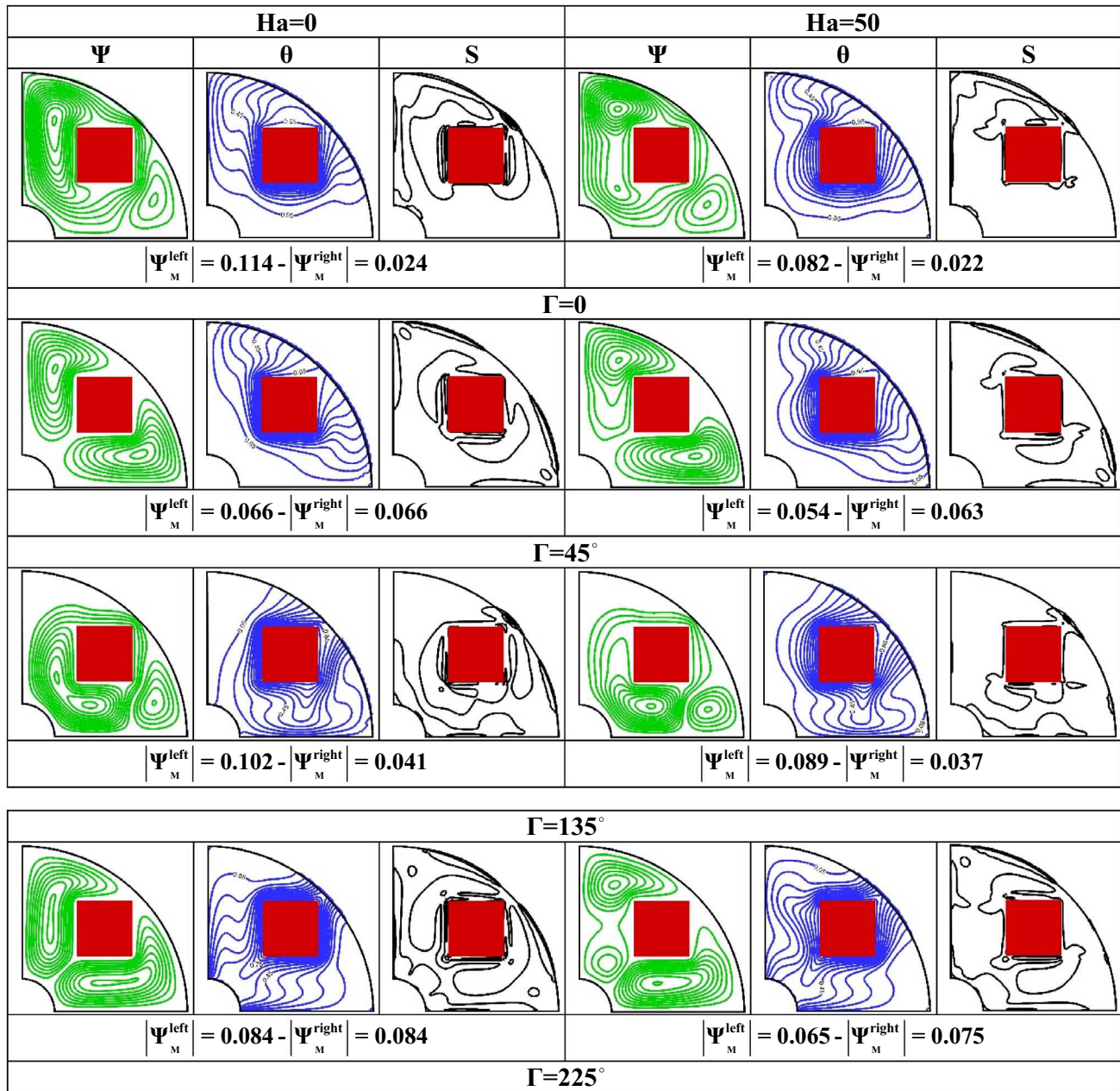


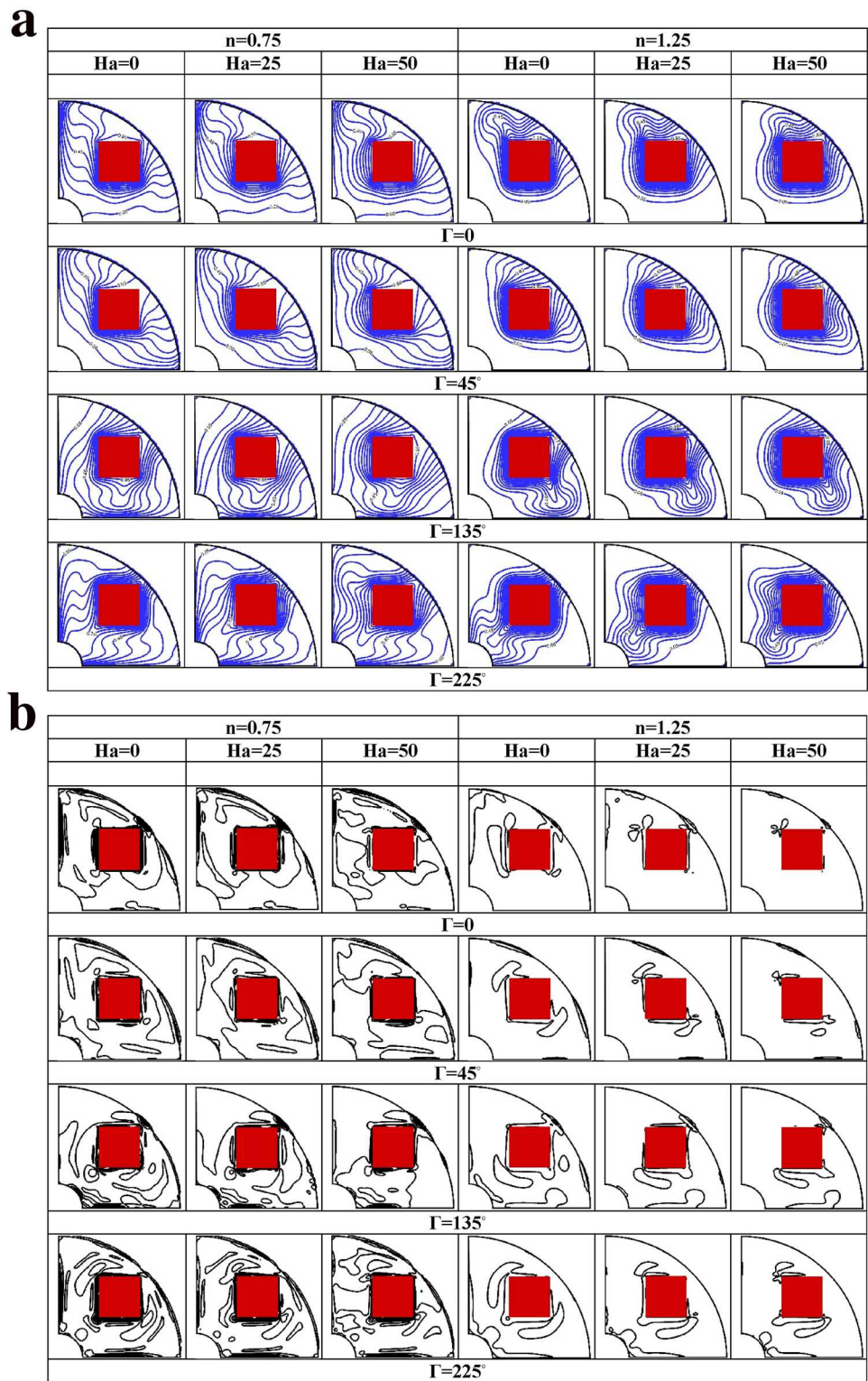
Fig. 6 The flow patterns at  $n=1, m=3, \varphi=0.02, RP=0.25, \Delta=0, \lambda=90^\circ, D2, Ra=10.5$

density near the heat generating object decreases, leading to the creation of two vortices of the same size in the opposite direction of rotation. For  $\Gamma=0$  and  $\Gamma=135^\circ$ , there is a main vortex, while a secondary vortex is formed in the opposite direction, which reduces the strength of the main rotation (especially for  $\Gamma=0$ ). According to  $Ha=50$ , it can be observed that the application of MF can be used to control the current. Besides the change in the shape of the streamlines, the reduction of the maximum value of the streamlines is another effect of the MF application. This phenomenon can be justified according to Eqs. (9) and (10). Where the

MF weakens the effect of buoyancy by introducing a resisting force. The absence of symmetry in the flow patterns for  $\Gamma=45^\circ$  and  $\Gamma=225^\circ$  in  $Ha=50$  is justified on the basis that MF does not affect the entire volume of the chamber and is only applied to the enclosure middle third.

Taking into account Figs. 6 and 7a simultaneously, the analysis of the effect of changing the fluid PL index and the exerted MF strength for changes in the  $\Delta$  parameter on the isotherms is more tangible. Since the natural convection phenomenon occurs only due to the heating and cooling of the cavity walls without the influence of any

**Fig. 7 a** The isotherms at  $m=3$ ,  $\varphi=0.02$ ,  $RP=0.25$ ,  $\Delta=0$ ,  $\lambda=90^\circ$ ,  $D2$ ,  $Ra=10^5$ . **b** The entropy lines at  $m=3$ ,  $\varphi=0.02$ ,  $RP=0.25$ ,  $\Delta=0$ ,  $\lambda=90^\circ$ ,  $D2$ ,  $Ra=10^5$



other factors, the wall placement position is extremely important according to the direction of the gravity force. Four important points need to be described: 1—According to the location of the hot object near the large curved wall of the chamber, more space for nanofluid is placed under

the hot object for  $\Gamma=0$  and  $\Gamma=45^\circ$ . The small curvature of the isotherms and placement parallel to the walls of the chamber illustrate that the convection effects are reduced and thermal conductivity prevails. 2—According to the cavity placement shape under the gravity field effect, the

highest accumulation of isotherms occurs on the cold walls for  $\Gamma = 135^\circ$  and  $\Gamma = 225^\circ$ , and in this way, the highest amount of HT can be anticipated at these two angles. 3—Changing the fluid type and its effects on the flow characteristics is possible by changing the  $n$  criterion. According to Eq. (18), the increase of the shear force on the nodes is the result of the increase of the  $n$  index. This factor leads to an increase in fluid viscosity, which leads to the formation of a thermal boundary layer. This phenomenon is clearly evident for  $n = 1.2$ . The presence of the thermal boundary layer leads to a decrease in the concentration of isotherms on the cold walls. Increasing the accumulation of isotherms on the hot body, reducing dispersion, and a small distribution of isotherms on the surface of the chamber are the results of increasing the viscosity of the fluid with the PL model. 4—Inflicting a resistive force (Lorentz force) on the flow by increasing the Ha value reduces the isotherm gradient and causes conduction to prevail over convection. The reduction of these effects can be clearly observed by enhancing the  $n$  parameter.

By viewing Figs. 6 and 7b concurrently, the lowest value of the distribution of entropy lines belongs to  $\Gamma = 45^\circ$ . This case can be justified by the lower power of the streamlines and convection effects according to isotherms. The higher concentration of entropy lines in the vicinity of the cold walls and the hot body (especially in  $\Gamma = 225^\circ$ ) is very evident. The increase of the  $n$  parameter and the Ha value according to Eqs. (14)–(17) has a decreasing effect on the GE value. Because the gradients of temperature and speed are constituent elements of entropy, the enhancement of these two parameters leads to the decrement of these values.

The decrease in the flow speed due to the increase in the nanofluid viscosity caused by increasing the  $n$  parameter is revealed in Fig. 8a due to horizontal velocity. The reduction of the maximum speed value by about 74% due to the enhancement of the  $n$  index exhibits that the effects

of convection are greatly reduced. The decreasing effect of enhancing the Ha value on flow speed is visible in Fig. 8b due to vertical velocity. Because, according to Eqs. (9) and (10), the Lorentz force acts against gravity force and reduces the movement speed of the nanofluid within the enclosure. Figure 8c discloses that by placing the chamber at an angle of 45 degrees, the nanofluid temperature changes linearly until it reaches the temperature of the hot component. The absence of temperature curvature in the profile is a justification for the low convection effects, unlike  $\Gamma = 225^\circ$ . For  $X < 0.2$ , where there is a cold wall, the temperature of the nanofluid is highest for  $\Gamma = 225^\circ$ . This factor reveals more cooling of the hot body for this angle.

According to what was described in Fig. 7a, the highest/lowest amount of heat exchange between the hot object and the cavity cold walls occurs for  $\Gamma = 225^\circ/\Gamma = 45^\circ$ , respectively. In addition, the percentage reduction of the mean Nu value for growth of the Ha value is the lowest for  $\Gamma = 45^\circ$  (about 18%) based on Fig. 9a. By changing the  $\Gamma$  parameter, in addition to attaining a different the Nu value, the effectiveness of changing the  $n$  parameter can be managed, as displayed in Fig. 9b. In  $\Gamma = 45^\circ$ , enhancing the  $n$  parameter from 1 to 1.2 has no noticeable change in the mean Nu value, while this effect is important for other  $\Gamma$  values. The decrease in the mean Nu value due to the increase in the  $n$  parameter is caused by the decrease in fluid speed due to the increase in viscosity, as was clear in Fig. 8a. By changing the type of fluid from the shear thinning ( $n = 0.8$ ) to the shear thickening ( $n = 1.2$ ), the mean Nu values for  $\Gamma = 0$ ,  $\Gamma = 45^\circ$ ,  $\Gamma = 135^\circ$  and  $\Gamma = 225^\circ$  drop by about 66%, 51%, 69% and 75%, respectively. The increase in the value of the  $n$  index diminishes the effect of MF. Because the increase in viscosity reduces the intensity of fluid movement inside the cavity, which itself causes a reduction in convection effects. According to Fig. 9c, if high effectiveness of applied MF is desired, it is necessary to choose the shear thinning fluid

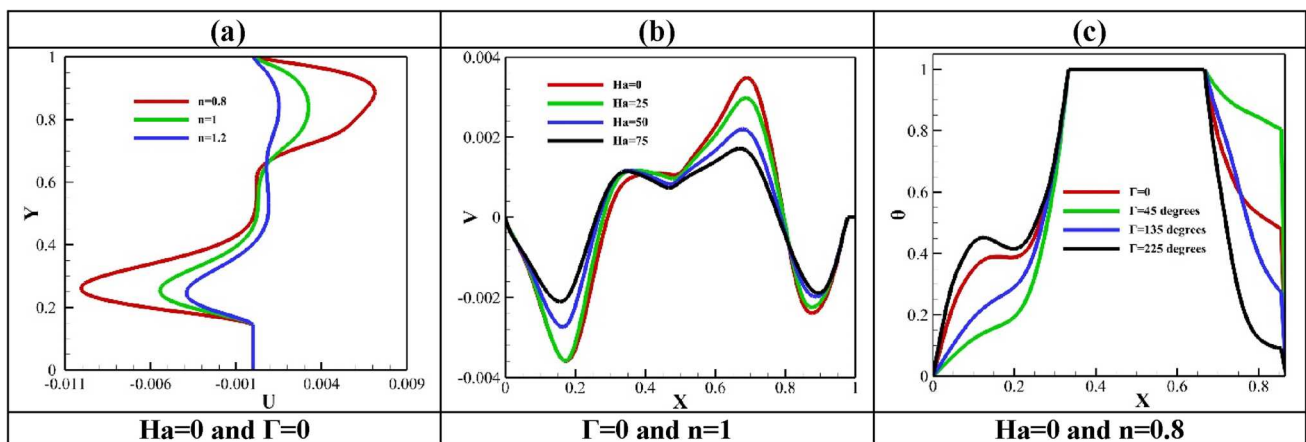


Fig. 8 Dimensionless of velocity and temperature at  $m = 3$ ,  $\varphi = 0.02$ ,  $RP = 0.25$ ,  $\Delta = 0$ ,  $\lambda = 90^\circ$ ,  $D2$ ,  $Ra = 10^5$

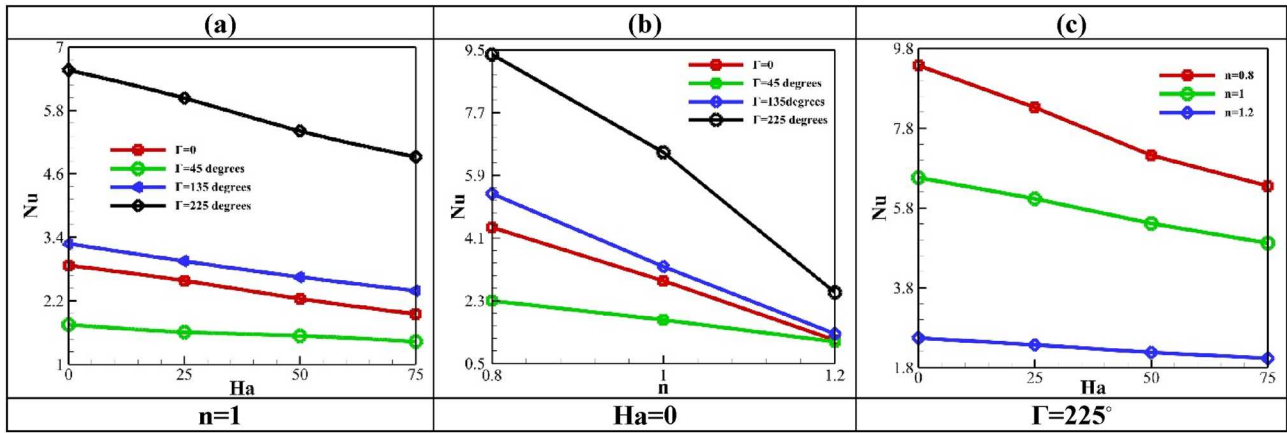


Fig. 9 The mean Nu values at  $m=3$ ,  $\varphi=0.02$ ,  $RP=0.25$ ,  $\Delta=0$ ,  $\lambda=90^\circ$ ,  $D2$ ,  $Ra=10^5$

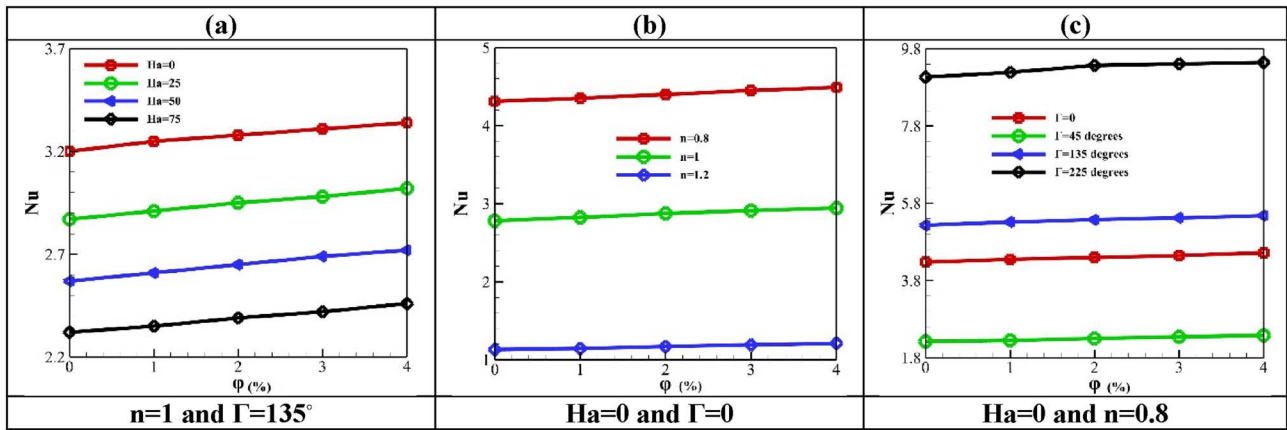


Fig. 10 The mean Nu values at  $m=3$ ,  $RP=0.25$ ,  $\Delta=0$ ,  $\lambda=90^\circ$ ,  $D2$ ,  $Ra=10^5$

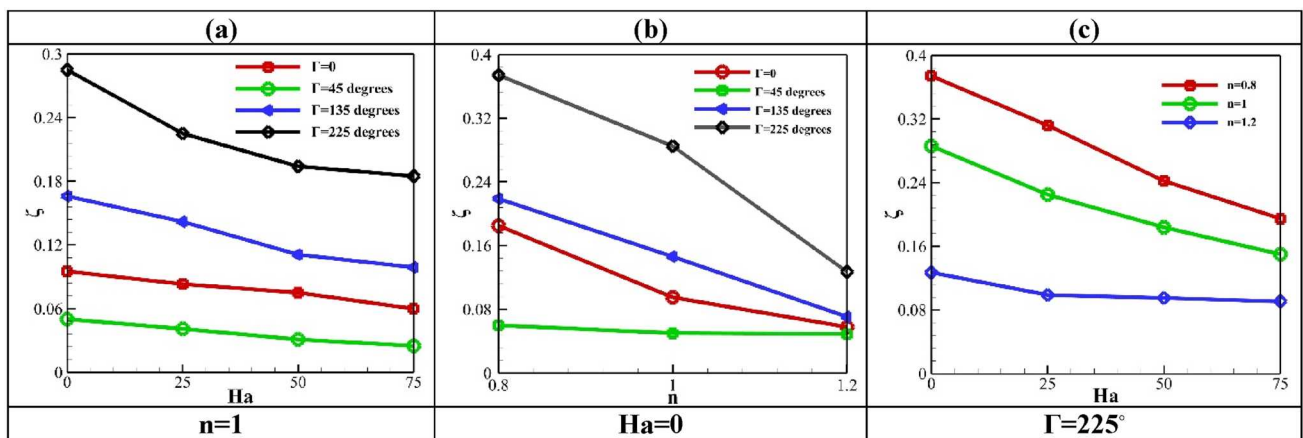


Fig. 11 The values of thermal performance index at  $m=3$ ,  $\varphi=0.02$ ,  $RP=0.25$ ,  $\Delta=0$ ,  $\lambda=90^\circ$ ,  $D2$ ,  $Ra=10^5$

to attain a larger mean Nu value. In general, it is clear from Fig. 9 that to decline the barrier temperature, it is better to select the shear thinning fluid ( $n=0.8$ ) as the working fluid in the absence of MF and for  $\Gamma=225^\circ$ .

Considering Fig. 10, adding nanoparticles to the pure fluid enhances the mean Nu value due to the improvement of the fluid thermal conductivity. In general, in cases where convection effects are less, adding nanoparticles and enhancing the volume fraction of these particles improves HT more clearly.

The trend of changes in the  $\zeta$  index is similar to the mean Nu value, according to Fig. 11. In the sense that the contribution of HT is the largest in the system's thermal characteristics, GE is the sum of three factor: HT, MF, and fluid friction, so the contribution of the other two factors except HT is very small. Three important points about Fig. 11: 1—For  $\Gamma=45^\circ$ , a change in the type of fluid does not cause a specific change in the value of  $\zeta$ , which may be due to the low

effect of convection in this state. This shows that the amount of entropy reduction is proportional to the amount of mean Nu value reduction. 2—According to  $n=1.2$ , the enhancement of the Ha value to more than 25 does not change the value of  $\zeta$  because, in this case, thermal conductivity prevails over convection (it can be justified by looking at Figs. 6 and 7). 3—The best thermal performance and the highest HT occur at  $\Gamma=225^\circ$ , and this can be considered in the design of the cooling system.

Depending on which areas of the chamber are affected by the imposed MF, the values of the flow characteristics will be different. As can be seen provided in Fig. 12, due to more space on the left side of the chamber, there is a larger clockwise vortex in this area, and a smaller anti-clockwise vortex is created on the left side. Depending on the direction and area of the exerted MF, the streamlines undergo visible changes for different Hartmann values, especially for  $\lambda=0$  and D3. Because, according to Eqs. (9)

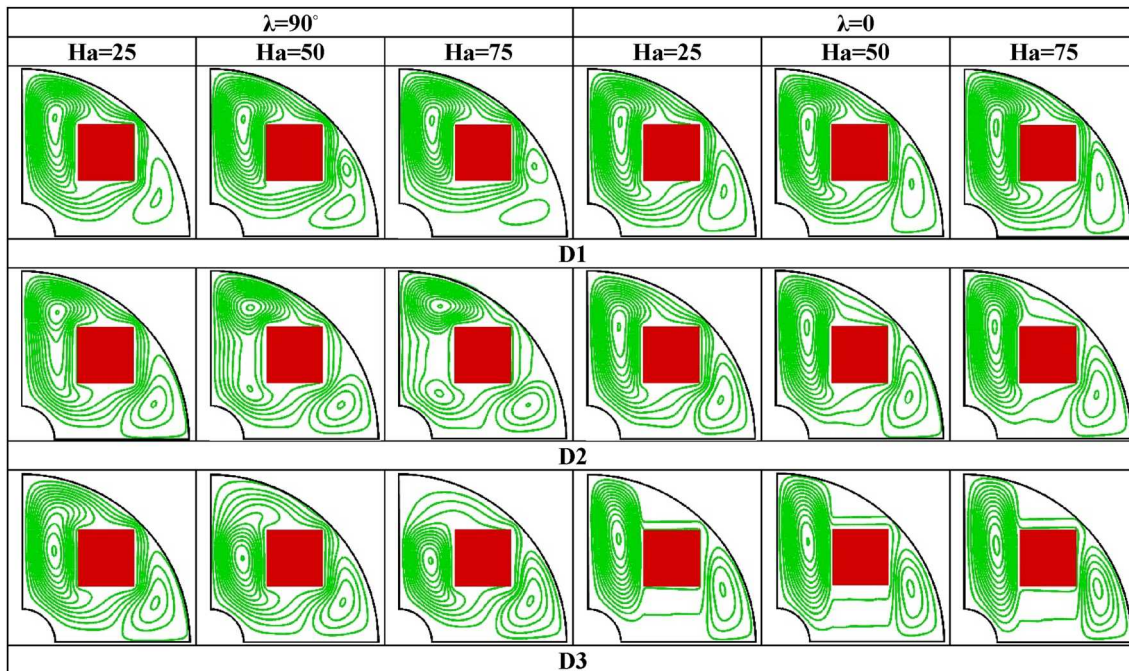


Fig. 12 The streamlines at  $m=3, \Gamma=0, \varphi=0.02, RP=0.25, \Delta=0, n=1, Ra=10^5$

Table 5 The maximum strength of the current formed inside the chamber at  $m=3, \Gamma=0, \varphi=0.02, RP=0.25, \Delta=0, n=1, Ra=10^5$

	$\lambda=90^\circ$						$\lambda=0$					
	$ \psi_M^{left} $			$ \psi_M^{right} $			$ \psi_M^{left} $			$ \psi_M^{right} $		
	D1	D2	D3	D1	D2	D3	D1	D2	D3	D1	D2	D3
Ha=0	0.114	0.114	0.114	0.024	0.024	0.024	0.114	0.114	0.114	0.024	0.024	0.024
Ha=25	0.112	0.099	0.103	0.015	0.023	0.024	0.109	0.104	0.085	0.018	0.024	0.019
Ha=50	0.108	0.082	0.088	0.011	0.022	0.024	0.106	0.098	0.07	0.014	0.023	0.018
Ha=75	0.104	0.073	0.079	0.009	0.021	0.023	0.103	0.094	0.054	0.011	0.023	0.018

and (10), the horizontal imposition of MF introduces a reducing force to the momentum equation in the  $Y$  direction, while for the horizontal application of MF, a resisting force is added to the momentum equation in the  $X$  direction. It is feasible to have a better understanding of changing the application area and the MF angle according to Table 5. According to  $\lambda = 90^\circ$ , the greatest reduction in the strength of vortices with enhanced the Ha values is for D2 (around 29%), while this effect is only around 5.5% for D1. Because when the MF is inflicted on the first third of the chamber, the convection forces are weak due to the location of the hot barrier on top of the cold wall. This information can be deduced from the isotherms for  $n = 1$  and  $\Gamma = 0$  in Fig. 6. In the first third part of the chamber, in the direction of  $Y$ , no isotherm density is observed, which depicts that convection effects are low. According to  $\lambda = 0$ , the most effective MF occurs in reducing the maximum amount of streamlines for D3, where the MF enters the first third of the chamber along the  $X$ -axis, because in this range, there are the highest convection effects, similar to the argument that was expressed about  $\lambda = 90^\circ$ .

According to Fig. 13, the decrease in the distribution and dispersion of the isotherms, which is obtained by increasing the Ha value, is a little more noticeable for horizontally applied the MF. Because in this case, the force resulting from MF acts exactly against gravity force, to make the effect of changing the position of applying MF more obvious, it is indispensable to grow the Ha value. The greater concentration of isotherms around the hot

object creates the view that the cooling of the hot object declines with an increment of the Ha value.

The same effect, as the imposed MF area on the isotherms in Fig. 13, is evident on the entropy lines in Fig. 14. The greatest effect of the imposed MF (obvious reduction of entropy lines, especially around the hot object) is attained when the middle third of the enclosure for  $\lambda = 90^\circ$ , and the first third of the enclosure for  $\lambda = 0$  are placed against MF. An increment of the Ha value greatly declines the accumulation of entropy lines on the walls, and only entropy lines density can be seen around the hot obstacle caused by the temperature difference.

According to Fig. 15, for  $\lambda = 0$ , the decrease of only 4.2% of the average Nu value for enhancing the Ha value from zero to 75 at D1 is justified due to the lack of change in the shape of the isotherms in Fig. 13. While the effect of increasing the Ha value increases by moving the applied MF position away from the large adiabatic curved wall (about 31% for D3). For  $\lambda = 90^\circ$ , a decrease of 11%, 19%, and 33% of the average Nu value is obtained based on the justifications presented in Fig. 13.

The ratio of the average Nu value to the total GE value ( $\zeta$ ) in Fig. 15 divulges several important points: 1—The reduction of the  $\zeta$  parameter in both applied MF angles is imposed on the cooling system. From this trend of changes, it is inferred that the effect of increasing the Ha index has a greater effect on the reduction of the HT rate compared to the reduction of entropy. 2—For  $\lambda = 0$ , exactly the same trend as for the average Nu value is also present for the  $\zeta$

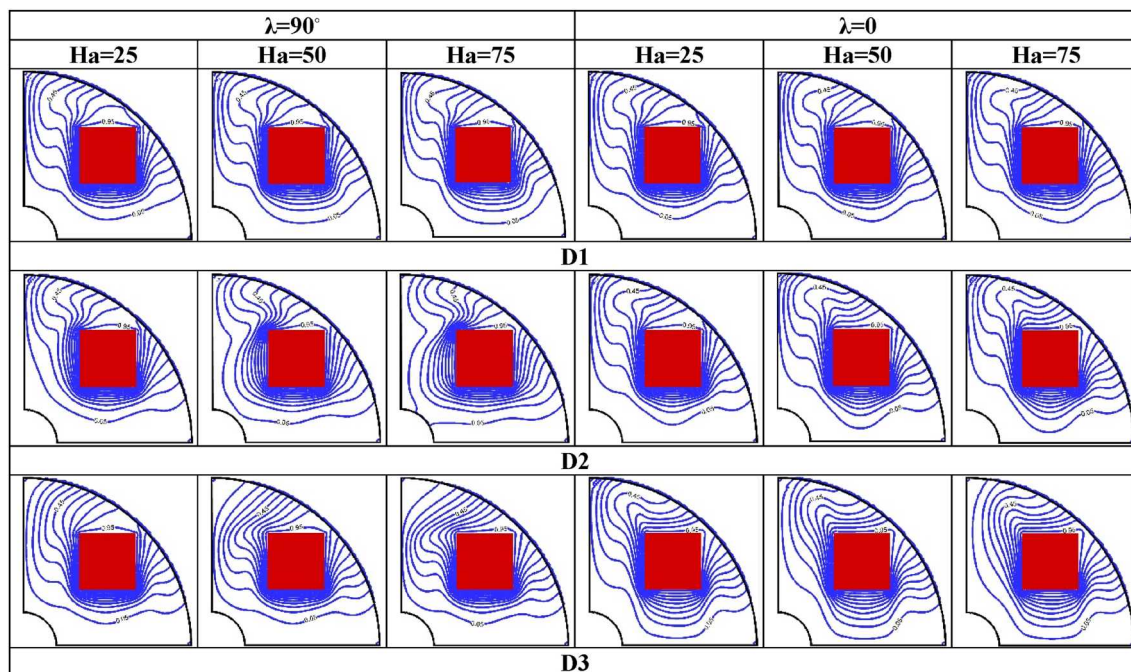


Fig. 13 The isotherms at  $m = 3, \Gamma = 0, \varphi = 0.02, RP = 0.25, \Delta = 0, n = 1, Ra = 10^5$

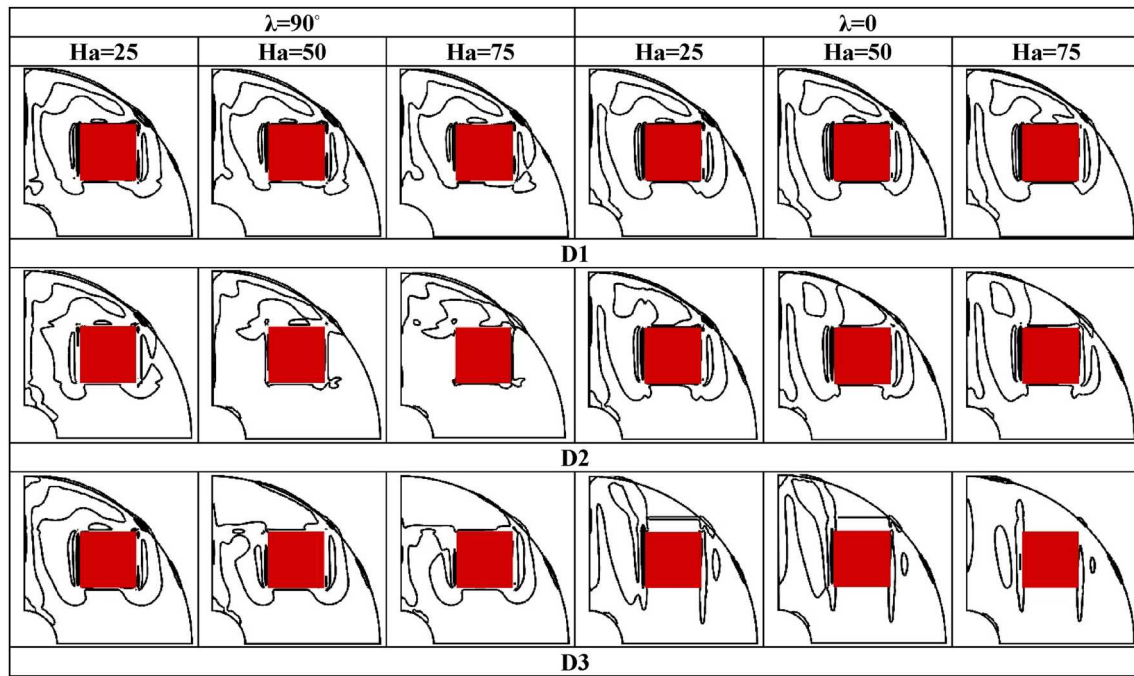


Fig. 14 The entropy lines at  $m=3$ ,  $\Gamma=0$ ,  $\varphi=0.02$ ,  $RP=0.25$ ,  $\Delta=0$ ,  $n=1$ ,  $Ra=10^5$

parameter. However, at  $\lambda=90^\circ$ , more reduction of the mean Nu value compared to the reduction of entropy is observed for the growth of the Ha value at D3. From the information in Fig. 15, it can be taken advantage of that if there is forced MF, to increase the cooling performance, at  $\lambda=0$ , it is better to apply MF to the last third of the chamber, while for  $\lambda=90^\circ$ , MF should be exerted on the first third.

The increase in the temperature gradient in the vicinity of the cavity cold walls as a result of the increase in buoyancy forces (increase in the Ra value) is depicted in Fig. 16. An increase in the nonlinear distribution of isotherms indicates an increase in convection effects, which is obtained by enhancing the Ra value. As the Ra value enhances based on Eqs. (9) and (10), the volumetric force injected into the fluid flow is strengthened. By applying heat absorption, the created heat sink causes more accumulation of isotherms on the hot object, and according to the law of the energy conservation, the isotherms density on the cold walls diminishes in the same proportion. So enhancing the heat absorption coefficient has a negative effect on the cooling of the hot object. The reduction of irreversibility for enhancing the  $\Delta$  parameter is another important result. By comparing parts (a) and (b) of Fig. 16, the sharp decrease of the GE, especially around the chamber walls, due to the enhancement of the  $n$  parameter for  $Ra=10^5$  and  $Ra=10^6$  is wholly witnessed. Because in these cases, the influence of enhancing the  $n$  parameter in reducing the flow speed is the maximum value possible, the important point is that the heat absorption phenomenon is less effective for enhancing

the Ra value, to the point where for  $n=1.2$  and  $Ra=10^6$ , enhancing  $\Delta$  parameter is almost ineffective on the entropy lines and isotherms.

This issue can be clearly understood according to Fig. 17 where the temperature profiles in terms of the  $\Delta$  parameter changes in  $Ra=10^6$ , are almost identical. Another important point about Fig. 17 is the reduction of temperature in the near of the cavity cold wall to increase the value of the heat absorption coefficient.

To get a better understanding of the effect of enhancing the Ra values and the heat absorption coefficient, the average Nu value is disclosed in Fig. 18. Part (a) in Fig. 18 clears that for all the values of the  $n$  index, the highest/lowest value of the average Nu belongs to  $Ra=10^6$ / $Ra=10^4$ , while the greatest effect of fluid type change is exhibited for  $Ra=10^5$ . By reducing the isotherm dispersion on the cold walls of the chamber, as revealed in Fig. 16, it is obvious to reduce the amount of the mean Nu value. It is possible to reduce the effect of heat absorption by changing the fluid type, which is determined in part (b) in Fig. 18. With the average Nu value criterion, a 86% reduction in the HT value for the shear thinning fluid can be achieved, compared to a 66% reduction for the Newtonian fluid and a 35% reduction for the shear thickening fluid. According to Fig. 18 in part (c), the fall in the effectiveness of heat absorption with the enhancement of the Ra values is clearly visible. The 35% decrease in the average Nu value for increasing the heat absorption coefficient for  $Ra=10^6$  compared to the 97% decrease for  $Ra=10^4$  clears

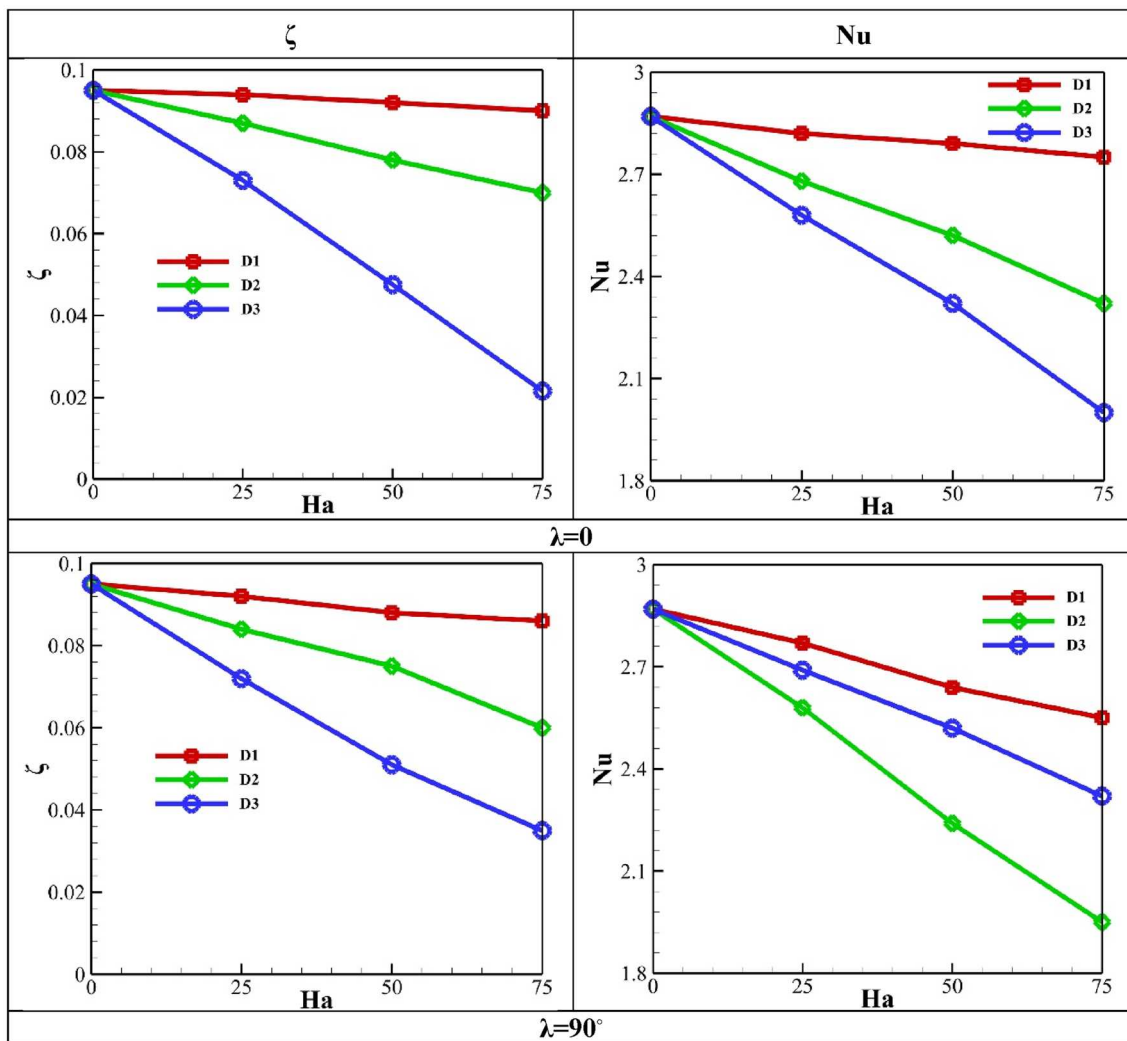


Fig. 15 The mean Nu value and index of thermal performance at  $m=3$ ,  $\Gamma=0$ ,  $\varphi=0.02$ ,  $RP=0.25$ ,  $\Delta=0$ ,  $n=1$ ,  $Ra=10^5$

that for  $Ra=10^6$  the buoyancy and convection forces are so strong that this internal factor has a limited effect.

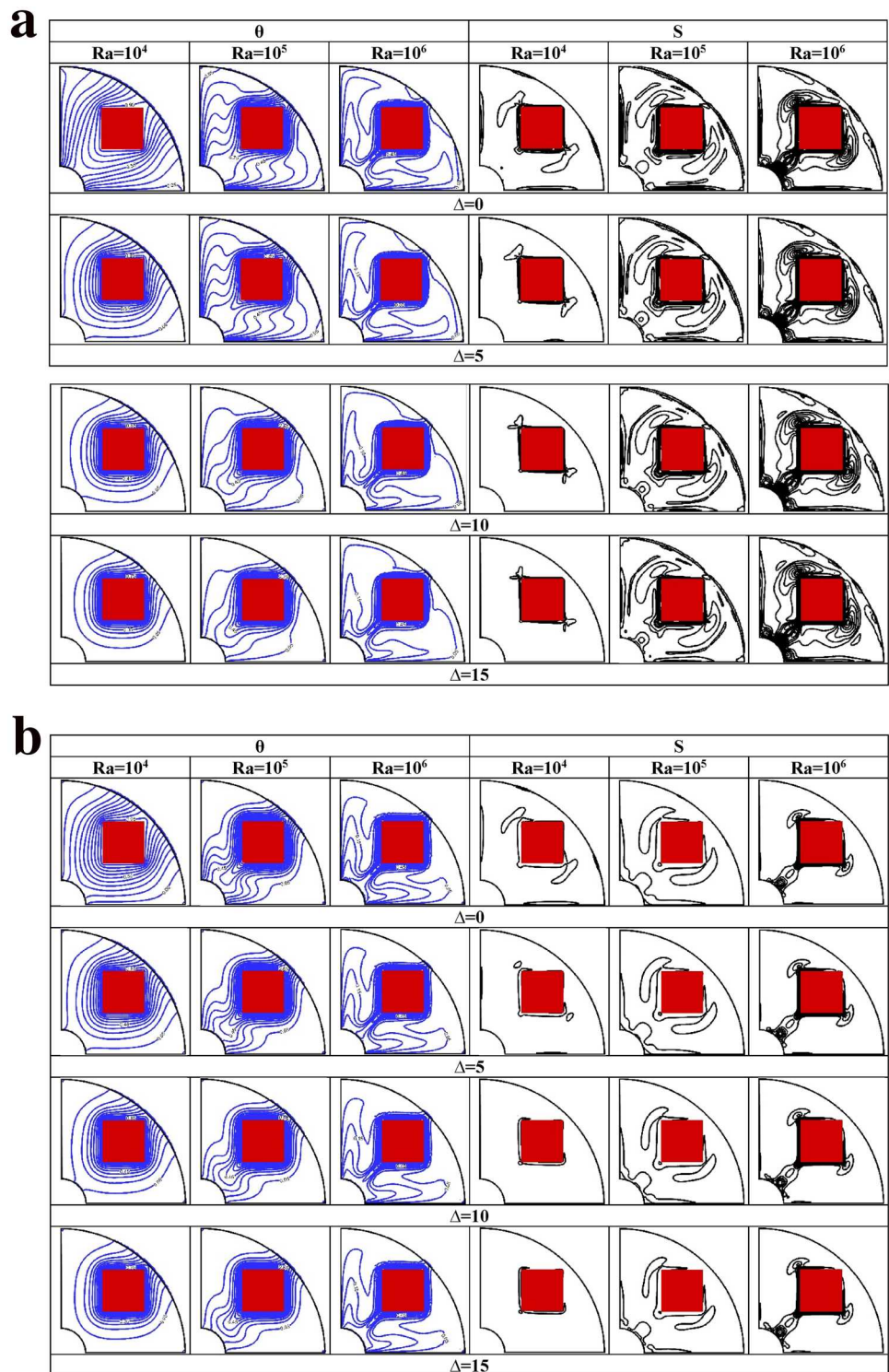
Considering the powerful convection effects in  $Ra=10^6$ , although the average Nu value depicts a decreasing trend with the increment of the  $n$  parameter, according to Fig. 18a, but according to Fig. 19a, the changes in the  $\zeta$  index with the enhancement of the  $n$  parameter are trivial. The higher  $\zeta$  index in  $Ra=10^5$  compared to  $Ra=10^6$  indicates that although a larger the Nu value is obtained for the highest Ra value, it also leads to higher entropy. A similar behavior with the Nu value for the cooling thermal performance index can be seen in Figs. 19b and c.

According to Fig. 20a, enhancing in the share of HT in the entropy formation is the result of the increase in the heat absorption coefficient. Because, as seen in Fig. 16, the power of convection is greatly reduced due to heat absorption, for this reason, the share of MF and fluid friction also decreases with the increment of the  $\Delta$  parameter. For  $\Delta=15$ , compared

to the case without heat absorption, the Be value enhances by about 24%. The opposite effect of increasing the heat absorption coefficient on the entropy contribution factors can be seen for increasing the Ra value in Fig. 20b. The reason for this is the increase in the strength of the buoyancy force with the growth of the Ra value. The fluid can move with greater force at  $Ra=10^6$ , and in this way, the velocity value and velocity gradient (entropy generating factors due to fluid friction and MF) grow. The increase in the Be value due to the increase of the  $n$  parameter is inferred from Fig. 20c due to the dominance of thermal conduction over thermal convection.

Increasing the volume fraction of nanoparticles according to Eq. (13) leads to an improvement in the thermal conductivity coefficient, which causes the value of the mean Nu value to increase as shown in Fig. 21a. This effect is more pronounced when the conduction is dominant over thermal convection (especially in  $Ra=10^4$ ). For  $Ra=10^6$ , although

**Fig. 16 a** The flow patterns at  $n=0.8$ ,  $m=3$ ,  $\Gamma=225^\circ$ ,  $\varphi=0.02$ ,  $RP=0.25$ ,  $Ha=0$ . **b** The flow patterns at  $n=1.2$ ,  $m=3$ ,  $\Gamma=225^\circ$ ,  $\varphi=0.02$ ,  $RP=0.25$ ,  $Ha=0$



the value of the average Nu has a relative increase up to  $\varphi=0.02$ , there is a decrease in the HT rate for  $\varphi > 0.02$ . The reason for this issue is the increase in viscosity due to the increase in the percentage of nanoparticles (pay attention to Eq. (1)). Therefore, one cannot always expect an increase in HT rate due to an increase in the  $\varphi$  parameter. According

to  $Ra=10^5$  in Fig. 21b, for all values of the heat absorption coefficient, the increase in the percentage of nanoparticles leads to an improvement in the HT rate. In  $\Delta=15$ , in the case where thermal conductivity is the dominant mechanism of HT, the improvement of HT by increasing the  $\varphi$  parameter to 0.04 is about 7.05%, while for  $\Delta=5$ , this effect is

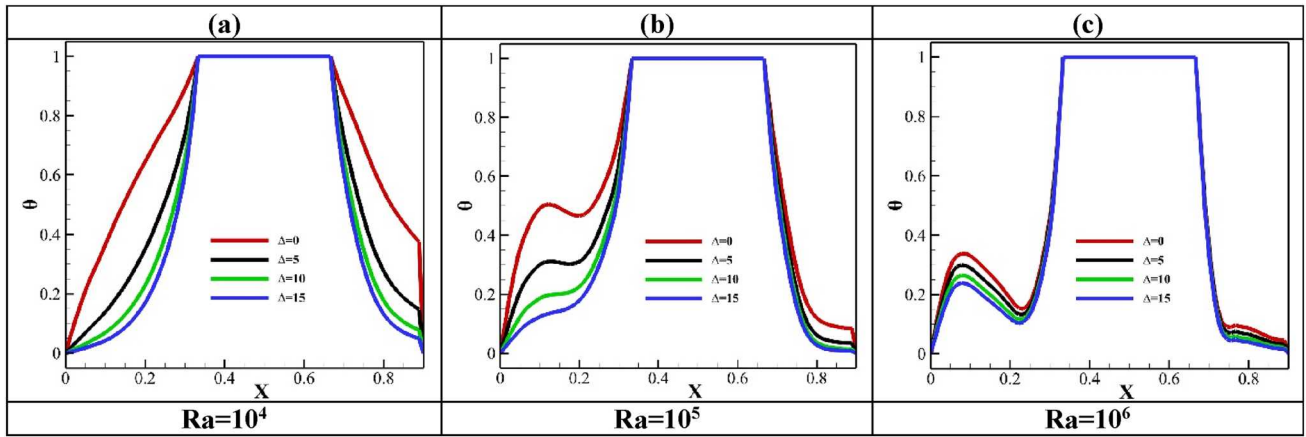


Fig. 17 Dimensionless temperature at  $n=0.8, m=3, \Gamma=225^\circ, \varphi=0.02, RP=0.25, Ha=0$

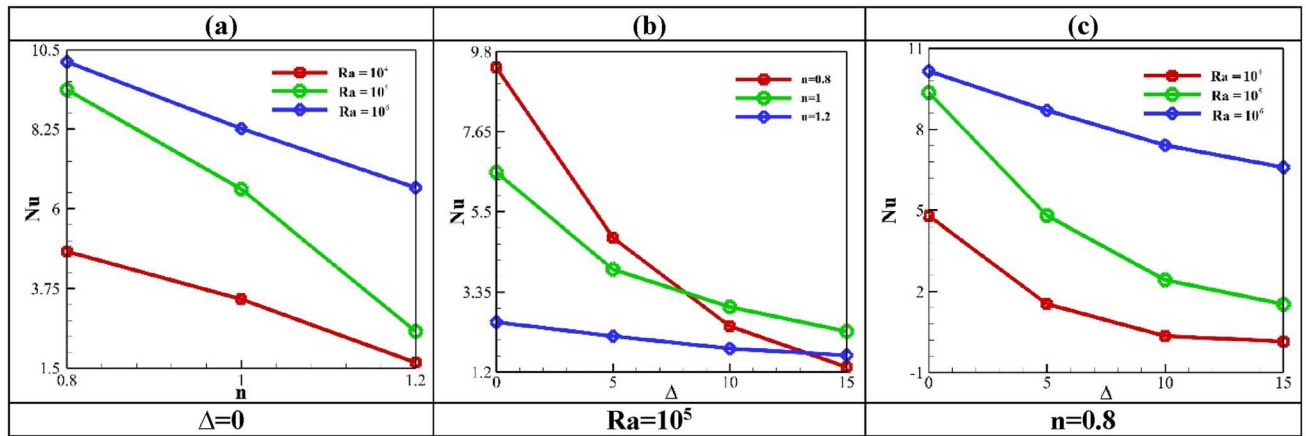


Fig. 18 The mean Nu value at  $m=3, \Gamma=225^\circ, \varphi=0.02, RP=0.25, Ha=0$

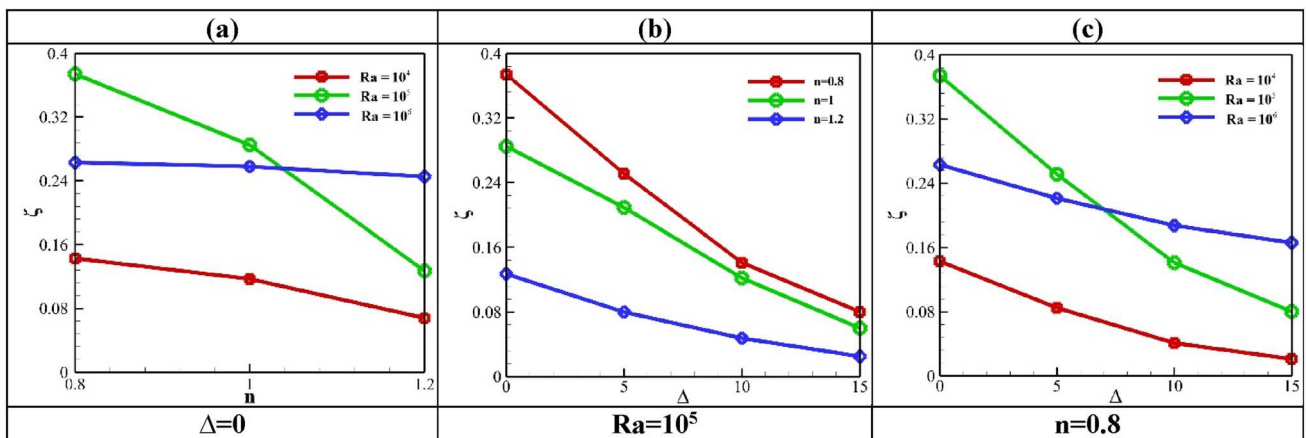


Fig. 19 The values of thermal performance index at  $m=3, \Gamma=225^\circ, \varphi=0.02, RP=0.25, Ha=0$

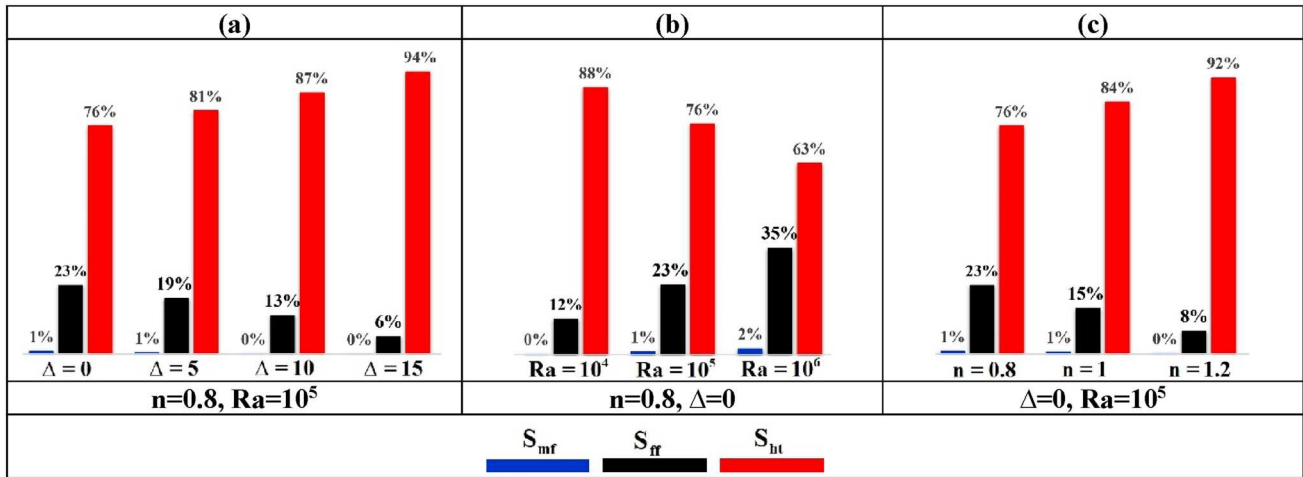


Fig. 20 The contribution percentage of each the factors in GE at  $m=3$ ,  $\Gamma=225^\circ$ ,  $\varphi=0.02$ ,  $RP=0.25$ ,  $Ha=50$ ,  $D2$ ,  $\lambda=90^\circ$

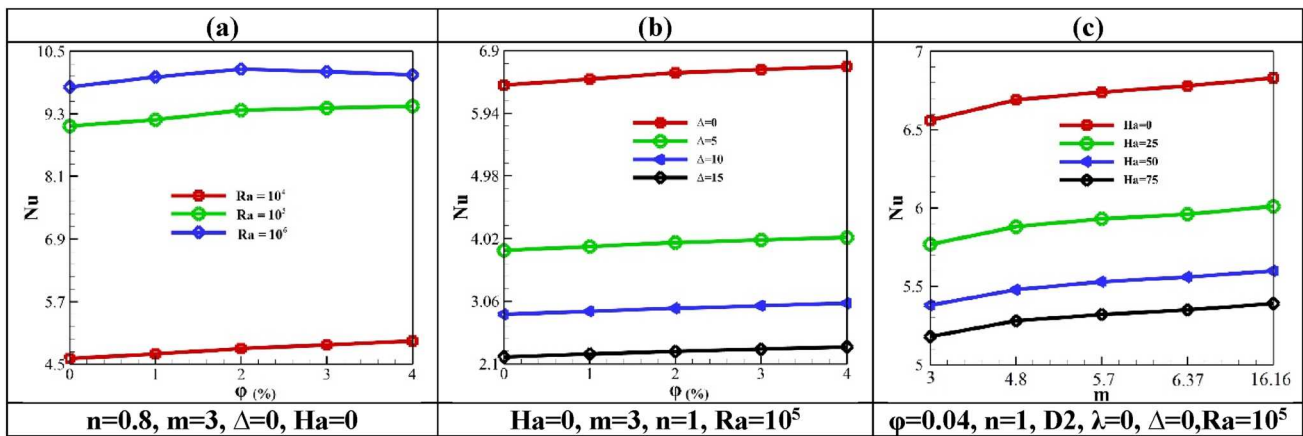


Fig. 21 The mean Nu value at  $\Gamma=225^\circ$ ,  $RP=0.25$

about 5.2%. Changing the shape of the nanoparticle results in a larger mean Nu value due to higher thermal conductivity. According to Fig. 21c, by changing the shape of the nanoparticle from spherical ( $m=3$ ) to lamina ( $m=16.16$ ), the Nu value improves by about 4.2%. Because, according to the Eq. (7), of the enhancement of the  $m$  coefficient, the thermal conductivity coefficient is obtained more. Because of the enhancement of the  $m$  parameter, the contact surface of nanoparticles increases in interaction with the base fluid. Since there is no nanoparticle shape factor parameter in determining the electrical conductivity coefficient of nanofluid according to Eq. (6), the trend of the average Nu value changes with increasing the Ha value is decreasing and similar for all values of the  $m$  parameter.

The investigation of isotherms behavior under the simultaneous effect of heat absorption parameter, the Ra value and the Ha value is presented in Fig. 22. In  $Ra=10^4$ , the presence of MF has a negligible effect on the isotherms

to the extent that the ineffectiveness of MF imposition is quite clear for  $\Delta=15$ . By increasing the Ra value, due to the strengthening of convection, the effect of MF can be seen more clearly, in such a way that the accumulation of isotherms around the cold walls is declined and this density enhances on the hot object.

The effect of reducing the convection power caused by the low Ra value can be observed in diminishing the effectiveness of MF according to Fig. 23a. The average Nu value for  $Ra=10^4$  decreases only by about 12% with the enhancement of the Ha value, so the maximum effect is for  $Ha=25$ . According to Fig. 23b, enhancing the Ha value with the  $\Delta$  index changes the same behavior as the Ra changes. Decreasing both  $\Delta$  and the Ha parameters disturbs the cooling of the hot body due to reducing the effects of convection. Since the value of the Nu and the value of the total GE are dependent on the changes in speed and temperature gradient, it is not far-fetched to observe a trend similar to the mean Nu

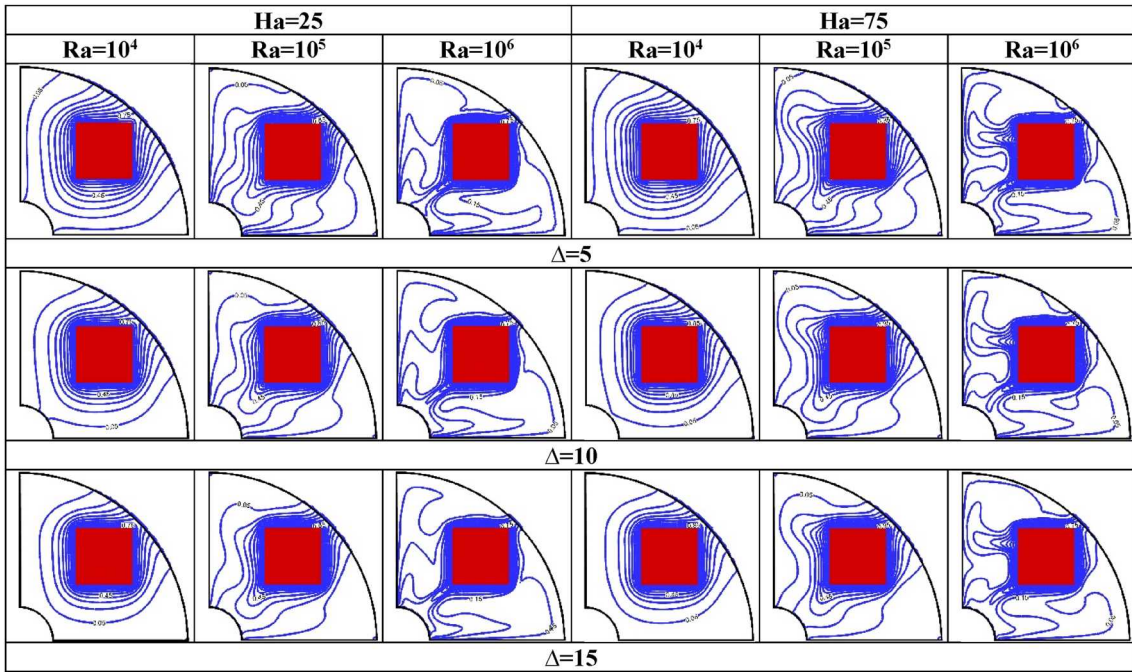


Fig. 22 The isotherms at  $m=3$ ,  $D2$ ,  $\lambda=90^\circ$ ,  $\Gamma=225^\circ$ ,  $\varphi=0.02$ ,  $RP=0.25$ ,  $n=0.8$

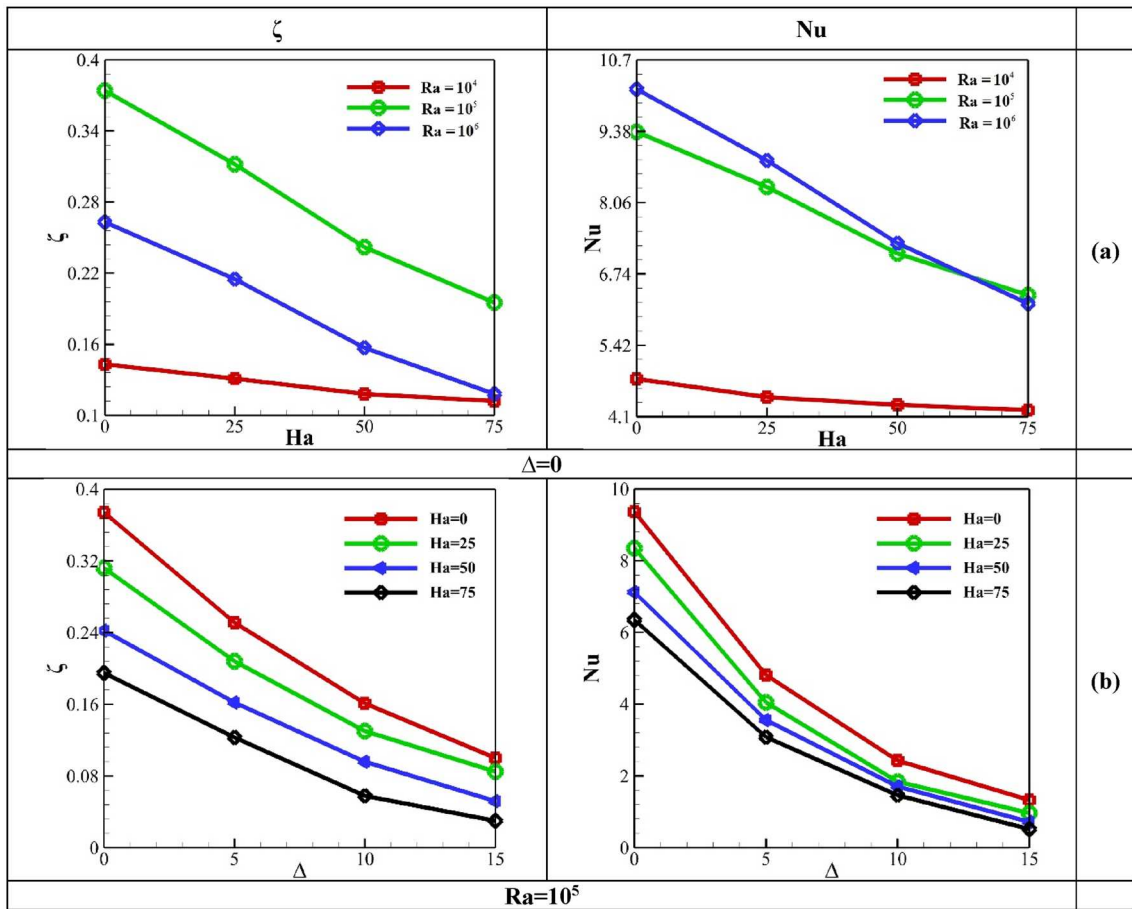


Fig. 23 The mean Nu value and index of thermal performance at  $m=3$ ,  $D2$ ,  $\lambda=90^\circ$ ,  $\Gamma=225^\circ$ ,  $\varphi=0.02$ ,  $RP=0.25$ ,  $n=0.8$

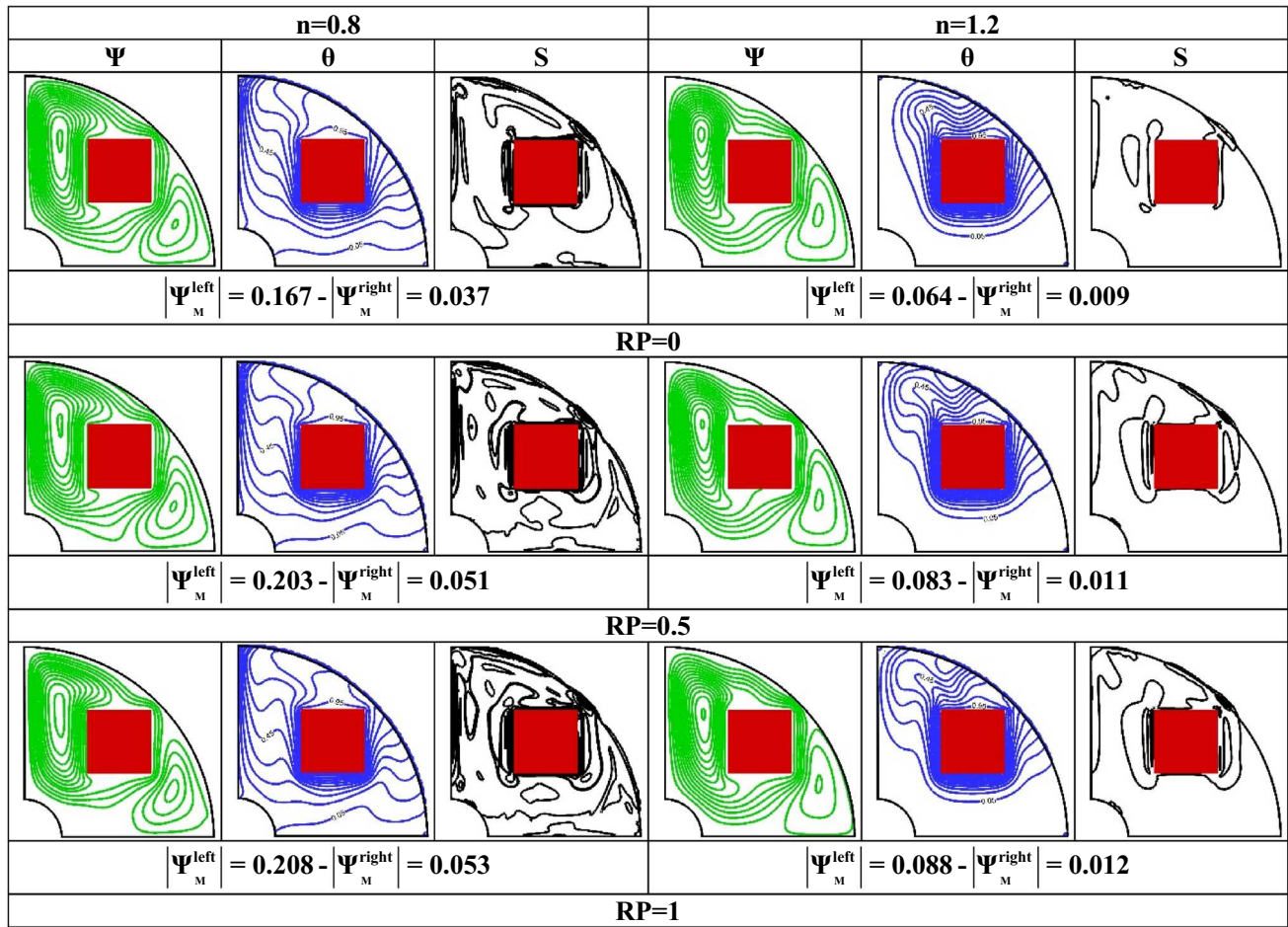


Fig. 24 The flow patterns at  $m=3, \Delta=0, \Gamma=0, \varphi=0.02, Ha=0, Ra=10^5$

value for the  $\zeta$  parameter, as seen in Fig. 23a. Because at the low Ra value, the flow ability to create stronger convection is not possible, the amount of impact that the MF creates for the large Ra values is not seen for  $Ra=10^4$ . Further decrease

of the average Nu value and the  $\zeta$  parameter due to increase of the Ha value and the  $\Delta$  parameter can be observed in Fig. 23b because both are strong reducing factors of cooling.

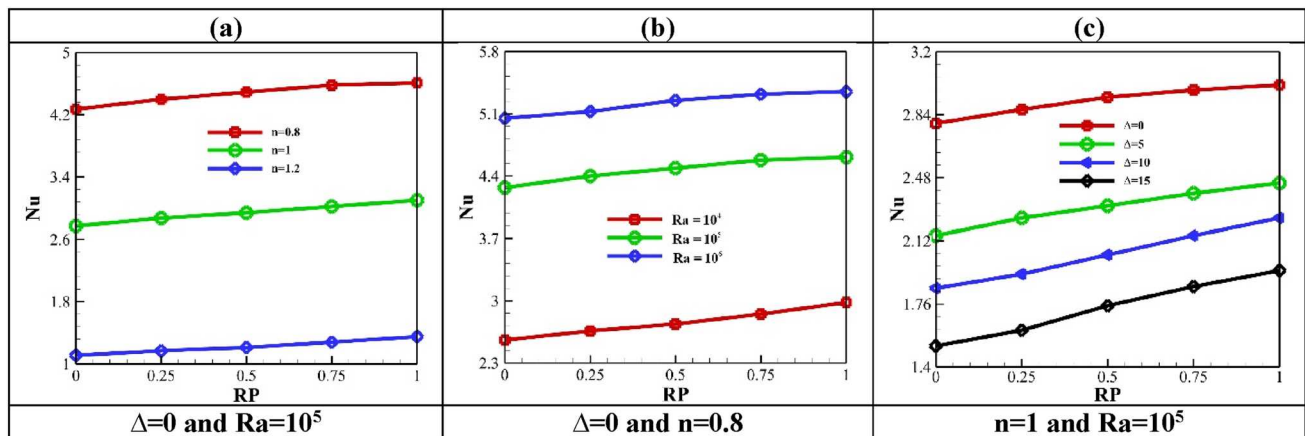


Fig. 25 The mean Nu value at  $m=3, \Gamma=0, \varphi=0.02, Ha=0$

According to Fig. 24, which shows the flow patterns for  $n=0.8$  and  $n=1.2$  at different values of the RP, the increase in the speed and power of the current inside the chamber is evident through the increase in the kinetic energy of the fluid due to the presence of radiation. Because adding radiation to the flow inside the chamber adds a new variable to the energy equation, according to the mutual dependence of the energy equation and the momentum equation, enhancing the value of the RP leads to an increase in the power of the flow. Due to the effect of enhancing the RP on the isotherms, the curvature and density of the lines are increased, especially in the hot object side area, which in turn leads to an increase in the HT amount. The increase in temperature and velocity gradients is the result of enhancing the value of the RP, which causes an increase in the irreversibility value in the hole of the cavity (especially around the hot body). The important point is the increase in flow power and the increase in isotherm curvature due to the increase in the RP for  $n=1.2$ , while the increase in the entropy density is greater for  $n=0.8$ .

A similar behavior is observed for all three parts of Fig. 25 for the RP changes in different values of other parameters. The addition of radiation to the NCHT, in addition to enhancing the speed and power of the flow, leads to an improvement in the average Nu value. Figure 25 reveals the fact that in order to reduce the effects of convection, the effectiveness of adding the radiation term grows more significantly. Increasing the slope of the graphs for reducing the Ra value and enhancing the  $\Delta$  coefficient confirms this fact. For example, according to Fig. 25a, the effect of adding radiation is more evident due to the increase of fluid viscosity, as explained in Fig. 24. Because by enhancing the  $n$  parameter, the effects of convection are greatly reduced, and the addition of the radiation term leads to the strengthening of convection. A 17% increase compared to a 9.5% increase in the average Nu value for increasing the RP from 0 to 1,

respectively, for  $n=1.2$  and  $n=0.8$  indicates the fact that the reduction of convection effects enhances the effectiveness of radiation.

Figure 26 presents a behavior similar to the average Nu value for TPI at changes in the RP due to changes in other variables. Three points can be explained: 1—For  $n=0.8$ , enhancing the RP value to more than 0.5 is not very effective on TPI. Because as the average Nu value increases due to the increase in the RP parameter, the creation of entropy intensifies to the same extent. In the low Ra values, the percentage enhancement of the Nu value for the growth of the RP value is higher than that of the GE value. So, one of the ways to control the effect of radiation is to change the strength of buoyancy forces. Because of the high Ra values, the intensity of convection is high. 3—The slope of enhancing the TPI amount is higher for increasing heat absorption coefficient. This is because the presence of radiation strengthens the RP mechanism by enhancing the introduction of more kinetic energy into the flow.

## 5 Conclusions

Investigating the improvement of the cooling performance of a hot body in a space limited to a tilted chamber filled with power-law ferrofluid under the effect of external and internal factors has been the target of this research. Parts that need to face temperature reduction in unwanted spaces and under special conditions to prevent damage and improve performance, setting up LBM with three separate distribution functions to model the velocity, temperature, and radiation fields in the presence of a magnetic field (uniform and non-uniform) and heat absorption in a specific geometry containing a fluid with radiation properties is one of the outstanding features of the present work. Similar to this study, with such a wide range of influencing parameters, it is very rare, and this

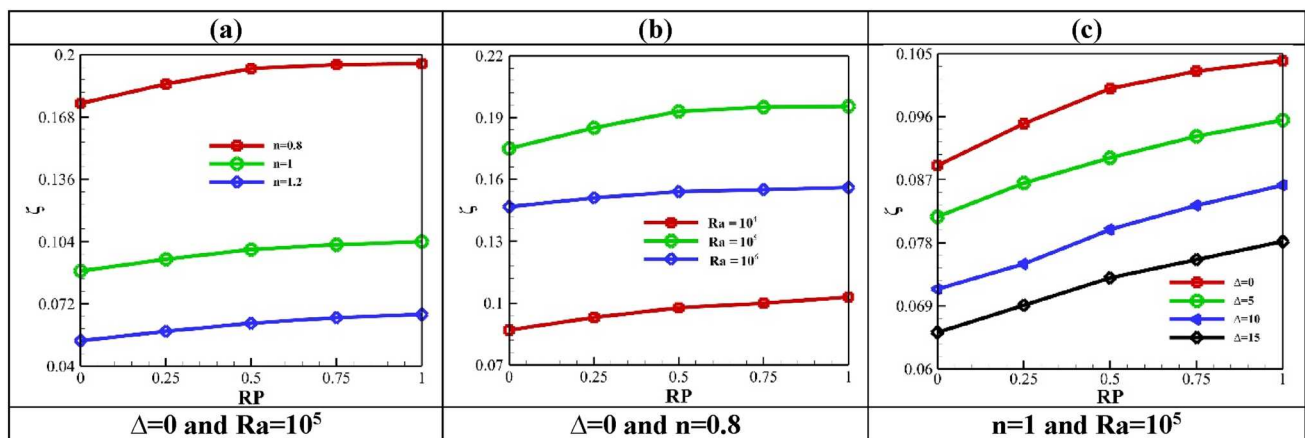


Fig. 26 The values of thermal performance index at  $m=3$ ,  $\Delta=0$ ,  $\Gamma=0$ ,  $\varphi=0.02$ ,  $Ha=0$

case is one of the highlights of the present study. The radiation parameter coefficient ( $RP=0-1$ ), the Hartmann Number value ( $Ha=0-75$ ), the position of applied magnetic field ( $D1-D3$ ), the heat absorption coefficient ( $\Delta=0-15$ ), the Rayleigh Number value ( $Ra=10^4-10^6$ ), the percentage of nanoparticles ( $0-0.05$ ), the chamber placement angle ( $0-225^\circ$ ), the fluid power-law index ( $n=0.8-1.2$ ), the applied magnetic field angle ( $\lambda=0, 90^\circ$ ) and the shape factor of nanoparticles ( $m=3-16.8$ ) are the investigated parameters with their corresponding values. It was shown that for  $\Gamma=45^\circ$ , there is the worst cooling performance of the hot component, and in this case, the effect of imposed MF is very small. To increase the impact of changing the fluid type (changing the  $n$  parameter), it is recommended to place the enclosure at  $\Gamma=225^\circ$  in  $Ra=10^5$  for  $\Delta=0$ . With the dominance of thermal conductivity via the enhancement of the heat absorption coefficient, the cooling performance and the effect of imposing MF diminish, while in this case, the influence of adding nanoparticles to the pure fluid in improving the HT rate enhances. Enhancing the Nu value and thermal performance by enhancing the RP parameter is more effective for situations where conduction dominates convection, especially for the shear thickening fluid. Depending on the angle of MF imposed on the chamber, by changing the position of applying MF, different thermal characteristics can be attained.

**Authors' Contribution** MN was involved in the project administration, writing, editing, formal analysis, methodology, conceptualization, writing—original draft; MS contributed to the formal analysis, methodology, conceptualization, and supervision; TJ assisted in writing and editing; AC contributed to writing, editing and conceptualization.

**Funding** There is no funding source.

**Availability of Data and Materials** The data and material are available and can be presented in the case of needed.

## Declarations

**Conflict of interest** There is no conflict of interest.

**Ethical Approval** This article does not contain any studies with human participants or animals performed by any of the authors.

**Informed Consent** Informed consent was obtained from all individual participants included in the study.

## References

- Ali FH, Hamzah HK, Egab K, Arıcı M, Shahsavari A (2020) Non-Newtonian nanofluid natural convection in a U-shaped cavity under magnetic field. *Int J Mech Sci* 186:105887
- Ali L, Ali B, Ghori MB (2022) Melting effect on Cattaneo-Christov and thermal radiation features for aligned MHD nanofluid flow comprising microorganisms to leading edge: FEM approach. *Comput Math Appl* 109:260–269
- Almensorry MF, Hashim AS, Hamzah HK, Ali FH (2021) Numerical investigation of natural convection of a non-Newtonian nanofluid in an F-shaped porous cavity. *Heat Transf* 50(3):2403–2426
- Alrowaili D, Ahmed SE, Elshehabeey HM, Ezzeldien M (2022) Magnetic radiative buoyancy-driven convection of MWCNTs-C2H6O2 power-law nanofluids in inclined enclosures with wavy walls. *Alex Eng J* 61(11):8677–8689
- Aly AM, Raizah ZA (2020) Incompressible smoothed particle hydrodynamics simulation of natural convection in a nanofluid-filled complex wavy porous cavity with inner solid particles. *Phys A Stat Mech Appl* 537:122623
- Arulmozhi S, Sukkiramathi K, Santra SS, Edwan R, Fernandez-Gamiz U, Noeiaghdam S (2022) Heat and mass transfer analysis of radiative and chemical reactive effects on MHD nanofluid over an infinite moving vertical plate. *Results Eng* 14:100394
- Asha NE, Nag P, AkHTer MN, Molla MM (2023) MRT-lattice Boltzmann simulation of magnetic field effects on heat transfer from a heater in a C-shaped cavity filled with non-Newtonian hybrid nanofluids. *Int J Thermofluids* 18:100345
- Bai J, Hu X, Tao YH, Ji WH (2022) Investigation of non-Newtonian power-law free convection affected by a magnetic field in an inclined quarter-circle chamber containing the lozenge-shaped obstacle via MRT-LBM of first and second laws of thermodynamics. *Eng Anal Bound Elem* 145:335–351
- Barnoon P, Toghraie D, Karimpour A (2021) Application of rotating circular obstacles in improving ferrofluid heat transfer in an enclosure saturated with porous medium subjected to a magnetic field. *J Therm Anal Calorim* 145:3301–3323
- Butt ZI, Ahmad I, Shoaib M, Ilyas H, Raja MA (2023) A novel design of inverse multiquadric radial basis neural networks to analyze MHD nanofluid boundary layer flow past a wedge embedded in a porous medium under the influence of radiation and viscous effects. *Int Commun Heat Mass Transf* 140:106516
- Chamkha AJ, Dogonchi AS, Ganji DD (2018) Magnetohydrodynamic nanofluid natural convection in a cavity under thermal radiation and shape factor of nanoparticles impacts: a Numerical study using CVFEM. *Appl Sci* 8(12):2396
- Chammam W, Nazari S, Abbas SZ (2021) Numerical scrutiny of entropy generation and ferro-nanoliquid magnetic natural convection inside a complex enclosure subjected to thermal radiation. *Int Commun Heat Mass Transf* 125:105319
- Chen Z, Shu C (2020) Simplified lattice Boltzmann method for non-Newtonian power-law fluid flows. *Int J Numer Methods Fluids* 92(1):38–54
- Dogonchi AS, Armaghani T, Chamkha AJ, Ganji DD (2019) Natural convection analysis in a cavity with an inclined elliptical heater subject to shape factor of nanoparticles and magnetic field. *Arab J Sci Eng* 44:7919–7931
- Dong B, Zhou X, Zhang Y, Chen C, Li W (2018) Numerical simulation of thermal flow of power-law fluids using lattice Boltzmann method on non-orthogonal grids. *Int J Heat Mass Transf* 126:293–305
- Eichler P, Galabov R, Fučík R, Škardová K, Oberhuber T, Pauš P, Tintěra J, Chabiniok R (2023) Non-Newtonian turbulent flow through aortic phantom: experimental and computational study using magnetic resonance imaging and lattice Boltzmann method. *Comput Math Appl* 136:80–94
- Eid MR, Mabood F (2020) Two-phase permeable non-Newtonian cross-nanomaterial flow with Arrhenius energy and entropy generation: Darcy-Forchheimer model. *Phys Scr* 95(10):105209
- Filippova O, Hänel D (1998) Grid refinement for lattice-BGK models. *J Comput Phys* 147(1):219–228
- Guo Z, Zheng C, Shi B (2002) Discrete lattice effects on the forcing term in the lattice Boltzmann method. *Phys Rev E* 65(4):046308

- Ijaz Khan M, Alzahrani F (2021) Numerical simulation for the mixed convective flow of non-Newtonian fluid with activation energy and entropy generation. *Math Methods Appl Sci* 44(9):7766–7777
- Ilis GG, Mobedi M, Sunden B (2008) Effect of aspect ratio on entropy generation in a rectangular cavity with differentially heated vertical walls. *Int Commun Heat Ass Transf* 35(6):696–703
- Islam M, Hasan MF, Bhowmick S, Kamrujjaman M, Molla MM (2023) GPU-optimized LBM-MRT simulation of free convection and entropy generation of non-Newtonian power-law nanofluids in a porous enclosure at REV scale. *Int J Ambient Energy* 44(1):995–1016
- Jha BK, Samaila G (2023) Nonlinear approximation for buoyancy-driven mixed convection heat and mass transfer flow over an inclined porous plate with Joule heating, nonlinear thermal radiation, viscous dissipation, and thermophoresis effects. *Numer Heat Transf B Fundam* 83(4):139–161
- Kamis NI, Jiann LY, Shafie S, Rawi NA (2023) Numerical simulation of convection hybrid ferrofluid with magnetic dipole effect on an inclined stretching sheet. *Alex Eng J* 76:19–33
- Kashyap D, Dass AK, Oztop HF, Abu-Hamdeh N (2021) Multiple-relaxation-time lattice Boltzmann analysis of entropy generation in a hot-block-inserted square cavity for different Prandtl Numbers. *Int J Therm Sci* 165:106948
- Kebriti S, Moqtaderi H (2021) Numerical simulation of convective non-Newtonian power-law solid-liquid phase change using the lattice Boltzmann method. *Int J Therm Sci* 159:106574
- Khan NH, Paswan MK, Hassan MA (2022) Natural convection of hybrid nanofluid heat transport and entropy generation in cavity by using Lattice Boltzmann Method. *J Indian Chem Soc* 99(3):100344
- Khodabandeh E, Rozati SA, Joshaghani M, Akbari OA, Akbari S, Toghraie D (2019) Thermal performance improvement in water nanofluid/GNP-SDBS in novel design of double-layer micro-channel heat sink with siNusoidal cavities and rectangular ribs. *J Therm Anal Calorim* 136:1333–1345
- Li Z, Hussein AK, Younis O, Afrand M, Feng S (2020) Natural convection and entropy generation of a nanofluid around a circular baffle inside an inclined square cavity under thermal radiation and magnetic field effects. *Int Commun Heat Mass Transf* 116:104650
- Loenko DS, Shenoy A, Sheremet MA (2019) Natural convection of non-Newtonian power-law fluid in a square cavity with a heat-generating element. *Energies* 12(11):2149
- Malkeson SP, Alshaaaili S, Chakraborty N (2023) Numerical investigation of steady state laminar natural convection of power-law fluids in side-cooled trapezoidal enclosures heated from the bottom. *Numer Heat Transf A Appl* 83(7):770–789
- Mei R, Luo LS, Shyy W (1999) An accurate curved boundary treatment in the lattice Boltzmann method. *J Comput Phys* 155(2):307–330
- Mendu SS, Das PK (2021) Lattice Boltzmann modeling for natural convection in power-law fluids within a partially heated square enclosure. *J Heat Transf* 143(3):032601
- Mohebbi R, Ma Y (2023) Optimal configuration of discrete heat sources in a channel with sudden expansion and contraction by lattice Boltzmann method. *J Therm Anal Calorim* 148(10):4553–4566
- Mohebbi R, Delouei AA, Jamali A, Izadi M, Mohamad AA (2019) Pore-scale simulation of non-Newtonian power-law fluid flow and forced convection in partially porous media: thermal lattice Boltzmann method. *Phys A Stat Mech Appl* 525:642–656
- Mohebbi R, Abbaszade A, Varzandeh M, Ma Y (2021) Natural convection heat transfer of Ag-MgO/water micropolar hybrid nanofluid inside an F-shaped cavity equipped by hot obstacle. *J Heat Mass Transf Res* 8(2):139–150
- Mourad A, Abderrahmane A, Younis O, Marzouki R, Alazzam A (2022) Numerical simulations of magnetohydrodynamics natural convection and entropy production in a porous anNulus bounded by wavy cylinder and Koch snowflake loaded with Cu–water nanofluid. *Micromachines* 13(2):182
- Mousavi SM, Biglarian M, Darzi AA, Farhadi M, Afrouzi HH, Toghraie D (2020) Heat transfer enhancement of ferrofluid flow within a wavy channel by applying a non-uniform magnetic field. *J Therm Anal Calorim* 139:3331–3343
- Nemati M, Farahani SD (2023) Using lattice Boltzmann method to control entropy generation during conjugate heat transfer of power-law liquids with magnetic field and heat absorption/production. *Comput Part Mech* 10(3):331–354
- Nemati M, Sefid M (2023) Magnetohydrodynamics combined convection modeling via LBM for shear thinning nanofluids within an inclined enclosure: appraisal of heat transfer and entropy under the impact of various parameters. *Comput Part Mech* 10(4):965–989
- Nemati M, Sefid M, Karimipour A, Chamkha AJ (2023) Computational thermal performance analysis by LBM for cooling a hot oval object via magnetohydrodynamics non-Newtonian free convection by using magneto-ferrofluid. *J Magn Magn Mater* 577:170797
- Pordanjani AH, Vahedi SM, Aghakhani S, Afrand M, Öztop HF, Abu-Hamdeh N (2019) Effect of magnetic field on mixed convection and entropy generation of hybrid nanofluid in an inclined enclosure: sensitivity analysis and optimization. *Eur Phys J plus* 134:1–20
- Rahman A, Nag P, Molla MM, Hassan S (2021) Magnetic field effects on natural convection and entropy generation of non-Newtonian fluids using multiple-relaxation-time lattice Boltzmann method. *Int J Mod Phys C* 32(01):2150015
- Rahman A, Redwan DA, Thohura S, Kamrujjaman M, Molla MM (2022) Natural convection and entropy generation of non-Newtonian nanofluids with different angles of external magnetic field using GPU accelerated MRT-LBM. *Case Stud Therm Eng* 30:101769
- Rashid U, Lu D, Iqbal Q (2023) Nanoparticles impacts on natural convection nanofluid flow and heat transfer inside a square cavity with fixed a circular obstacle. *Case Stud Therm Eng* 44:102829
- Rezaie MR, Norouzi M (2018) Numerical investigation of MHD flow of non-Newtonian fluid over confined circular cylinder: a lattice Boltzmann approach. *J Braz Soc Mech Sci Eng* 40:1
- Safaei MR, Karimipour A, Abdollahi A, Nguyen TK (2018) The investigation of thermal radiation and free convection heat transfer mechanisms of nanofluid inside a shallow cavity by lattice Boltzmann method. *Phys A Stat Mech Appl* 509:515–535
- Saleem KB, Marafie AH, Al-Farhany K, Hussam WK, Sheard GJ (2023) Natural convection heat transfer in a nanofluid filled l-shaped enclosure with time-periodic temperature boundary and magnetic field. *Alex Eng J* 69:177–191
- Selimefendigil F, Chamkha AJ (2019) Magnetohydrodynamics mixed convection in a power law nanofluid-filled triangular cavity with an opening using Tiwari and Das' nanofluid model. *J Therm Anal Calorim* 135:419–436
- Sharma BK, Khanduri U, Mishra NK, Mekheimer KS (2023) Combined effect of thermophoresis and Brownian motion on MHD mixed convective flow over an inclined stretching surface with radiation and chemical reaction. *Int J Mod Phys B* 37(10):2350095
- Shehzad SA, Madhu M, Shashikumar NS, Gireesha BJ, Mahanthesh B (2021) Thermal and entropy generation of non-Newtonian magneto-Carreau fluid flow in microchannel. *J Therm Anal Calorim* 143:2717–2727
- Shekaramiz M, Fathi S, Ataabadi HA, Kazemi-Varnamkhasti H, Toghraie D (2021) MHD nanofluid free convection inside the wavy triangular cavity considering periodic temperature boundary condition and velocity slip mechanisms. *Int J Therm Sci* 170:107179
- Sobhani M, Tighchi HA, Esfahani JA (2018) Taguchi optimization of combined radiation/natural convection of participating medium

- in a cavity with a horizontal fin using LBM. *Phys A Stat Mech Appl* 509:1062–1079
- Sulochana C, Begum S, Kumar TP (2023) MHD mixed convective Non-Newtonian stagnation point flow over an inclined stretching sheet: numerical simulation. *J Adv Res Fluid Mech Therm Sci* 102(1):73–84
- Tazangi HR, Goharrizi AS, Javaran EJ (2021) Comparison of the rheological behavior of particulate suspensions in power-law and Newtonian fluids by combined improved smoothed profile-lattice Boltzmann methods. *Korea Aust Rheol J* 33(3):293–306
- Tighchi HA, Sobhani M, Esfahani JA (2018) Effect of volumetric radiation on natural convection in a cavity with a horizontal fin using the lattice Boltzmann method. *Eur Phys J plus* 133:1–8
- Tighchi HA, Sobhani M, Esfahani JA (2019) Lattice Boltzmann simulation of combined volumetric radiation/natural convection to consider optical properties of nanoparticles. *Radiat Phys Chem* 159:238–251
- Toghraie D, Mashayekhi R, Arasteh H, Sheykhi S, Niknejadi M, Chamkha AJ (2019) Two-phase investigation of water-Al<sub>2</sub>O<sub>3</sub> nanofluid in a micro concentric annulus under non-uniform heat flux boundary conditions. *Int J Numer Methods Heat Fluid Flow* 30(4):1795–1814
- Wahid NS, Arifin NM, Khashi'ie NS, Pop I (2023) Mixed convection MHD hybrid nanofluid over a shrinking permeable inclined plate with thermal radiation effect. *Alex Eng J* 66:769–783
- Wang L, Huang C, Yang X, Chai Z, Shi B (2019) Effects of temperature-dependent properties on natural convection of power-law nanofluids in rectangular cavities with sinusoidal temperature distribution. *Int J Heat Mass Transf* 128:688–699
- Yuan Z, Dong Y, Jin Z (2023) Numerical simulation of MHD natural convection and entropy generation in semicircular cavity based on LBM. *Energies* 16(10):4055
- Zainodin S, Jamaludin A, Nazar R, Pop I (2023) Effects of higher order chemical reaction and slip conditions on mixed convection hybrid ferrofluid flow in a Darcy porous medium. *Alex Eng J* 68:111–126
- Zhang R, Aghakhani S, Hajatzadeh Pordanjani A, Vahedi SM, Shahsavari A, Afrand M (2020) Investigation of the entropy generation during natural convection of Newtonian and non-Newtonian fluids inside the L-shaped cavity subjected to magnetic field: application of lattice Boltzmann method. *Eur Phys J plus* 135(2):1–29
- Zhao TH, Khan MI, Chu YM (2023) Artificial neural networking (ANN) analysis for heat and entropy generation in flow of non-Newtonian fluid between two rotating disks. *Math Methods Appl Sci* 46(3):3012–3030
- Zhou J, Ali MA, Alizadeh AA, Sharma K (2023) Numerical study of mixed convection flow of two-phase nanofluid in a two-dimensional cavity with the presence of a magnetic field by changing the height of obstacles with artificial intelligence: Investigation of entropy production changes and Bejan Number. *Eng Anal Bound Elem* 148:52–61

Springer Nature or its licensor (e.g. a society or other partner) holds exclusive rights to this article under a publishing agreement with the author(s) or other rightsholder(s); author self-archiving of the accepted manuscript version of this article is solely governed by the terms of such publishing agreement and applicable law.